

		ISSN 0016-7037 Volume 75, Number 5 March 1, 2011			
Geochimica et Cosmochimica Acta JOURNAL OF THE GEOCHEMICAL SOCIETY AND THE METEORITICAL SOCIETY					
EDITING EDITOR: FRANK A. PODOSEK		EDITORIAL MANAGER: LINDA THOMER EDITORIAL ASSISTANT: KAREN KLEIN KATHY SCHER			
WIREEDITOR: ROBERT H. NEUBER, JR. PRODUCTION MANAGER: CHRIS AUVER					
ASSOCIATE EDITORS:	ROBERT C. ALLEN ROBERT C. ALP YUKI ANDO CAROL ARONOW MAYUKA BABA-MATHIEWS LIANG G. BAI TOSHIO S. BANNO JAY A. BARNES ALAN E. BARRON DAVID J. BARRIE ROBERT H. BERRY WILLIAM H. CARO THOMAS CHAPIN JON CHAPMAN ANDRÉ CORRE CHRISTOPHER J. DICKHOUT	ZHONGQI DING JAMES FARQUHAR FRANÇOIS A. FERT EDMUND GARLAND SUSAN CHANSHAN ETIENNE N. GORODEZ JEROME R. HEAL H. ROBERT HURVY GORDON R. HULL SUDIP R. HUNG GREGORY F. HUNG JIAN HAN TOSHIO HIRAI TAKESHI ISHIZUKA KAZUO IRIKAWA KLAUS JAKOBSON	CHRISTIAN KÖRBER RUSDI KRÖGER SPENCER M. KRAEMER S. KRÖGER ALEXANDER N. KRETZ GABRIEL A. LAJTHA JOSIP LITJ THOMAS J. LIVING MICHAEL L. MACHENRY BERNARD MARET TOM MCCLELLAN ANDRÉS MARIN MARTIN A. MARINI JACK J. MCDONALD ALFONSO MOTTI BENO MAYER	HIROSHI NAGAIWA MAYUKA NISHIKI PATRICY A. OTTLEY ERIC H. OXBURGH DMITRY PANKOV SANDRA PIZZARELLO MARK RIBBI W. UWE RIBBESE PETER W. RICHARDS EDWARD M. RILEY KEVIN M. RYAN SARA S. RYDQVIST E. J. RYDQVIST TOMAS A. SCHAEFER JACQUES SCHIFF THOMAS J. SHAW	JIAN S. SHENBERG DONALD I. SPARKER DAPHNE A. SODERBERG MICHAEL J. TAYLOR PETER ULLMANN DORIS VANCE DAVID J. VAN DER BRUG ROBERT J. WALKER LILLIAN A. WALKER JOHN WOOD BOB A. WOODRILL CHUN ZHANG
Volume 75, Number 5		March 1, 2011			
Articles					
S. FREYHAUSER, C. VOGT, J. MOHRZYNNEK, M. SZLENKIEWICZ, M. KRÜGER, M. STEIGERT, H.-H. RICHINGS: Different types of methane monooxygenases produce similar carbon and hydrogen isotope fractionation patterns during methane oxidation	1173				
L. GANDOLFI, A.-S. PEREIRA, A. PROBST: Impact of nitrogenous fertiliser-induced proton release on cultivated soils with contrasting carbonate contents: A column experiment	1185				
C. CHIFFOLEAU, L. FULCO, S. TAYLOR: Vesicoid cosmic spherules from the South Pole Water Well and Transantarctic Mountains (Antarctica): A major and trace element study	1199				
B. C. CHRISTENSEN, H. GECKLER, C. M. MARGUARDT, A. BAUER, J. RÖMER, T. WANK, D. SCHILD, S. L. S. STIPP: Neptunium (NpO ₂) interaction with green rust, GR ₁	1216				
W. LIU, S. J. BOHLE, D. TERTEMALE, B. EICHMANN, J.-L. HAZEMANN, J. BRUGGER: Speciation and thermodynamic properties for cobalt chloride complexes in hydrothermal fluids at 35–440 °C and 600 bar: An <i>in-situ</i> XAS study	1227				
F. VILA, O. MONTENAR, A. KALT, T. LEUWIG: Implications of the serpentine phase transition on the behaviour of beryllium and lithium-boron of subducted ultramafic rocks	1249				
F. J. SPERA, M. S. GIBROSO, D. NEVENS: Structure, thermodynamic and transport properties of liquid MgSiO ₃ : Comparison of molecular models and laboratory results	1272				
D. GORMAN-LEWIS: Enthalpies of proton adsorption onto <i>Bacillus licheniformis</i> at 25, 37, 50, and 75 °C	1297				
C. Y. WANG, I. H. CAMPBELL, A. S. STEFANOV, C. M. ALLEN, I. N. BEREZEV: Growth rate of the preserved continental crust: II. Constraints from Hf and O isotopes in detrital zircon from Greater Russian Rivers	1308				
P. LINDAHL, R. AAMLI, Y. JIYU, P. WOODFORD, M. KEITH ROACH, M.-S. CHO: Sources of platinum to the tropical Northwest Pacific Ocean (1943–1999) identified using a natural coral archive	1346				
<i>Continued on outside back cover</i>					

This article appeared in a journal published by Elsevier. The attached copy is furnished to the author for internal non-commercial research and education use, including for instruction at the authors institution and sharing with colleagues.

Other uses, including reproduction and distribution, or selling or licensing copies, or posting to personal, institutional or third party websites are prohibited.

In most cases authors are permitted to post their version of the article (e.g. in Word or Tex form) to their personal website or institutional repository. Authors requiring further information regarding Elsevier's archiving and manuscript policies are encouraged to visit:

<http://www.elsevier.com/copyright>



Structure, thermodynamic and transport properties of liquid MgSiO₃: Comparison of molecular models and laboratory results

Frank J. Spera^{a,*}, Mark S. Ghiorso^b, Dean Nevins^a

^a Department of Earth Science, University of California, Santa Barbara, CA 93106, USA

^b OFM Research-West, 7336 24th Avenue NE, Seattle, WA 98115, USA

Received 29 July 2010; accepted in revised form 2 December 2010; available online 11 December 2010

Abstract

Liquid MgSiO₃ is a model for the Earth's magma ocean and of remnant melt present near the core–mantle boundary. Here, models for molten MgSiO₃ are computed employing empirical potential molecular dynamics (EPMD) and results are compared to published results including two EPMD studies and three first-principles molecular dynamics (FPMD) models and to laboratory data. The EPMD results derived from the Oganov (OG) potential come closest to the density of MgSiO₃ liquid at the 1-bar melting point inferred from the melting curve. At higher *P*, EPMD densities calculated from the OG potential and FPMD broadly match shock wave studies, with the OG potential yielding the better comparison. Matsui (M) potential results deviate from other studies above ~50 GPa. Overall, results based on the OG potential compare best to experimental densities over the *P*–*T* range of the mantle. Isothermally, upon increasing *P* the mean coordination numbers (CN) of oxygen around Si and Mg monotonically increase with pressure. Tetrahedral Si and octahedral Si monotonically increase and decrease, respectively, whereas pentahedral Si maximizes at 10–20 GPa. Tetrahedral Mg decreases monotonically as *P* increases whereas pentahedral, octahedral and higher coordination polyhedra each show similar behavior first increasing and then decreasing after attaining a maximum; the *P* of the maximum for each polyhedra type migrates to higher *P* as the CN increases. Free oxygen and oxygen with one nearest neighbor of either Si or Mg decreases whereas Si or Mg with two or three nearest oxygens (i.e., tricluster oxygen) increases with increasing *P* isothermally. The increase of tricluster oxygen is consistent with spectroscopy on MgSiO₃ glass quenched from 2000 K and 0–40 GPa and high-energy X-ray studies constraining the coordination of O around Mg and around Si at 2300 K and 1 bar. Coordination statistics from FPMD studies for O around Si and Si around O are in agreement with the EPMD results based on the M and OG potentials. Mg self-diffusivity is greater than O and Si self-diffusivities for both the M and OG potentials. All *D* values monotonically decrease with increasing pressure isothermally and all atoms are more diffusive in the M liquid compared to the OG liquid except at *T* > ~5000 K and *P* > 100 GPa. Previously published EPMD diffusivities fall between values given by the M and OG potentials, at least up to 45 GPa. The M liquid is generally less viscous than the OG liquid except at *P* > ~80 GPa. Activation energy and volume are around 96 kJ/mol and 1.5 cm³/mol, respectively. The FPMD viscosity results at 120 GPa and 4000 and 4500 K are essentially identical to the values from the M and OG potentials. FPMD viscosity results are similar to the OG results for *P* < 60 GPa; at higher *P*, the FPMD viscosities are higher. At 4000 K and 100 GPa the shear viscosity of liquid MgSiO₃ is ~0.1 Pa s. More extensive laboratory results are required to better define the thermodynamic, transport and structural properties of MgSiO₃ liquids and for comparison with computational studies.

© 2010 Elsevier Ltd. All rights reserved.

1. INTRODUCTION

The structure, thermodynamic and transport properties of natural silicate liquids over the pressure (*P*) and temperature (*T*) regime of the crust and mantle of Earth and other

* Corresponding author. Tel.: +1 805 893 4880; fax: +1 805 893 2314.

E-mail address: spera@geol.ucsb.edu (F.J. Spera).

terrestrial planets are pertinent to many outstanding geochemical and geophysical problems. For example, understanding mantle dynamics and the tectonic and thermal evolution of the Earth requires knowledge of the thermodynamics of melting and the transport properties of magma. Based on isotopic measurements (Halliday, 2008) and the dynamics of giant Moon-forming impact (Canup, 2004), it appears likely that the Earth's mantle was wholly or partly molten continuously or transiently during accretion and immediately following the giant Moon-forming impact. For Mars, isotopic data from Martian meteorites suggests that the source region of orthopyroxene cumulate ALH84001 underwent extensive igneous processing associated with crystallization of a deep magma ocean (Lapen et al., 2010). In general, short (~30–80 Myr) accretion times and the finite probability of giant impact during the latter stages of accretion favor development of magma oceans during planet formation. Indeed, magma oceans may be ubiquitous and there may be many hundreds of millions or more exoplanets in the Milky Way galaxy alone that undergo a magma ocean stage (Sasselov et al., 2008; Kite et al., 2009; Valencia and O'Connell, 2009). On Earth, it is possible that patches of melt remain along portions of the core–mantle boundary representing the fossil remnants of a former voluminous terrestrial magma ocean (Thorne and Garnero, 2004). Indeed, Labrosse et al. (2007) have argued that a stable layer of dense melt at the base of the mantle early in the Earth's history would be an ideal candidate for an unsampled geochemical reservoir required by ¹⁴²Nd/¹⁴⁴Nd isotopic data (e.g., Boyet and Carlson, 2005). Today, 4566 million years after the first solar system materials condensed to commence planetary accretion in the solar system, a volume of about 30 km³ of basaltic melt is generated in the upper mantle and emplaced or erupted each year (White et al., 2006). Magmatism therefore is and has been a fundamental part of the Earth's dynamic plate tectonic recycling process for more than 4.5 Gyr. Understanding the structure and properties of molten silicates is relevant to understanding Earth evolution and, by analogy, the parent bodies of the basaltic achondritic meteorites, the terrestrial planets of our solar system and possible terrestrial-type exoplanets around other stars.

Although accurate laboratory studies such as diamond-cell measurements, sinking sphere viscometry, sound speed measurements, phase equilibria, spectroscopy, diffusion and shock wave experiments represent the ultimate standard for determination of melt properties and structure, the range in composition, T (2000–5000 K) and P (0–135 GPa) relevant to multicomponent geological systems is enormous; it is too costly and time-consuming to study all possible compositions at the required range of state conditions in the laboratory. Fortunately, molecular dynamics (MD) simulation is a well-established and potent tool for investigating the structure and properties of a broad range of liquid compositions at many state points. Such results complement laboratory studies and enable rational extrapolation. In particular, MD methods can be used to develop thermodynamic equations of state (EOS) and parametric expressions for transport properties such as self-diffusivity (D), shear viscosity (η) and phonon conductivity (k), all extremely

useful in addressing geodynamic problems. Predictions based on modeling studies can be tested against laboratory measurements thereby leading to improvements in electronic structure calculations and empirical potentials sequentially and iteratively. The ultimate goal is to develop quantitative models for the properties of multicomponent silicate liquids spanning the P–T range relevant to terrestrial planet evolution consistent with experimental and theoretical constraints. There has already been success in the study of silicate liquids using this approach and even a cursory review of the computational literature applicable to high temperature liquids relevant to geochemical problems (magma end member compositions and molten iron) over the past thirty years reveals a rapid expansion in knowledge with accuracies comparable to experimental studies (e.g., Angell et al., 1982; Dempsey and Kawamura, 1984; Angell et al., 1987; Kubicki and Lasaga, 1990; Rustad et al., 1990; Della Valle and Andersen, 1992; Rustad et al., 1992; Poole et al., 1995; Stein and Spera, 1995; Bryce et al., 1998; Nevins and Spera, 1998; Morgan and Spera, 2001; Alfe et al., 2002; Stixrude and Karki, 2005; Guillot and Sator, 2007a,b; Lacks et al., 2007; Wan et al., 2007; de Koker et al., 2008; Ghiorso and Spera, 2009; Ghiorso et al., 2009; Martin et al., 2009; Nevins et al., 2009; Spera et al., 2009; Vuilleumier et al., 2009; de Koker, 2010). Research is accelerating due to the development of increasingly robust algorithms and the wide availability of computational engines. A recent review of some developments may be found in the collection of papers in Wentzcovitch and Stixrude (2010). Despite this progress there has been relatively little focus on direct comparison of FPMD studies to EPMD studies and of both to laboratory measurements.

The purpose of this study is to review what is known from both computation and laboratory experiment about the high temperature–pressure properties and structure of liquid MgSiO₃, an archetypical planetary molten silicate. Comparisons are made between properties and structures derived from three FPMD studies and four EPMD studies. In particular we compare EPMD results of Belonoshko and Dubrovinsky (1996, hereafter BD) and Lacks et al. (2007, hereafter LRO) based on potentials each author developed for the system MgO–SiO₂, to our MD results using the transferable potential of Matsui (1996, 1998 hereafter M) for the system Na₂O–CaO–MgO–Al₂O₃–SiO₂ and the compound-specific potential developed by Oganov et al. (2000, hereafter OG). These comparisons enable assessment of the sensitivity of computed properties and structure of MgSiO₃ on proposed interatomic pairwise additive potentials. We also compare the EPMD results to the FPMD studies of Stixrude and Karki (2005, hereafter SK), Wan et al. (2007, hereafter WDSC) and Vuilleumier et al. (2009, hereafter VSG) and then compare all computational studies to laboratory studies. Hence, we can explicitly evaluate FPMD calculations against three different EPMD potentials; one tailored to MgSiO₃, two for the binary system MgO–SiO₂ and one for the 5-component Na₂O–CaO–MgO–Al₂O₃–SiO₂ system. This comparison informs us regarding trade-offs between computational effort and quality of results. Although one may, in general, prefer FPMD results, an important question is when and at what level of

approximation are EPMD results useful given the wide range of relevant compositions that must be studied to develop models applicable to planetary geochemical systems? We will attempt to address this question in this paper and show that differences between results from different ‘first-principle’ studies can be as pronounced as those from EPMD simulations using alternate potentials. Although the fact that different methods can produce disparate results is expected if not well known, there are very few studies where these differences are made explicit particularly in the geochemical literature.

2. COMPUTATIONAL METHODS

Before addressing these questions, it is appropriate to briefly review details of the methods involved in first-principles and empirical potential molecular dynamics beginning with FPMD. In first-principles molecular dynamics (FPMD) the fundamental idea is to compute the forces acting on the nuclei from electronic structure calculations using, for example, Density Functional Theory (DFT) or the Hartree–Fock (HF) approach (e.g., Kohn and Sham, 1965; Parr and Yang, 1995; Meyer and Worth, 2003) performed ‘on-the-fly’ as the MD nuclei trajectory unfolds. The forces derived from the electronic structure are used with Newton’s equations to generate atomic trajectories and thence coordination statistics, the equation of state (EOS), self-diffusivities and other material properties based on standard prescriptions from macroscopic thermodynamics, statistical mechanics and linear response theory. There are several different flavors of FPMD with a large and rapidly expanding literature. The recent monographs by Marx and Hutter (2009) and Martin (2004) outline the state-of-the-art and make comparisons between the different flavors and approximations noting strengths and weaknesses and areas where improvements are being made. This is a very active branch of condensed-matter physics; the applications to geophysics and geochemistry are myriad. Here we just mention a few details related to the three FPMD studies drawn upon in this investigation so that a proper evaluation of comparisons can be made.

An advantage of FPMD of any flavor is that it is, in principle, an exact theory of many-body systems; empirical force fields used in EPMD are not required. Instead, complexity is hidden in the exchange–correlation functional, a component of the Kohn–Sham energy that forms the basis of DFT. Unfortunately, the form of this exchange–correlation functional is not known a priori and approximations must be invoked: a systematic approach for constructing exchange–correlation functionals of universal application remains elusive (Cohen et al., 2008). Although simple approximations often work and give useful results, different flavors of FPMD can generate different results that can have an impact on the application of results to answer or pose geochemical and geophysical problems. Three different FPMD studies are compared here.

SK implement a method called Born–Oppenheimer molecular dynamics embodied in the VASP code (Kresse and Furthmüller, 1996) using an 80 atom (16 formula units of MgSiO_3) system and run duration of 3 ps. In

Born–Oppenheimer MD, the static electronic structure problem is solved at each MD step for fixed nuclear positions (clamped nuclei) at each instant of time. The electronic structure is found by solving the time-independent Schrödinger equation while propagating the nuclei according to classical (Newtonian) mechanics. The total ground state energy of an interacting system of electrons with classical nuclei fixed is obtained as the minimum of the Kohn–Sham energy of DFT. There are two corrections made to the raw FPMD computed pressure in the work of SK. To account for the finiteness of the basis function set (energy cut-off of 400 eV), a temperature-independent but volume-dependant Pulay correction to FPMD pressure is made. The magnitude of the Pulay correction is 2 GPa at low pressure ($V/V_r = 1$) and 5 GPa when $V/V_r = 0.5$ where V_r is a reference volume taken as the molar volume of liquid MgSiO_3 at its incongruent ‘melting’ temperature of 1830 K at 1 bar (10^{-4} GPa). A second ‘empirical’ correction is also applied by adjusting the pressure +2 GPa uniformly (at all T). This constant pressure shift is applied to allow the computed liquid volume to agree with the experimental reference volume (Oganov et al., 2001; Wentzcovitch et al., 2004). The need for the empirical correction relates to the computation of the exchange–correlation energy. A critical part of the Kohn–Sham functional is the approximation of this unknown functional. In the simplest case, it is the exchange and correlation energy density of an interacting but homogeneous electron gas at the local density in the inhomogeneous system. This is the local density approximation (LDA) and has been called the first rung on “Jacob’s Ladder” leading upwards to the ‘divine’ functional (Perdew and Schmidt, 2001; Mattsson, 2002). LDA is associated with over binding of the electrons; hence the need for an empirical correction to the raw FPMD pressure. A good example of differences that can arise between the LDA and Generalized Gradient Approximation (GGA) pertinent to silicates is the computed relative stability of silica polymorphs α -quartz and stishovite. LDA predicts stishovite stable at low pressure whereas GGA (see below) leads to the correct result: α -quartz with lower energy (i.e., stable) at ambient pressure compared to stishovite (Hamann, 1996). This example illustrates how the choices one makes in FPMD can influence the outcome in non-trivial ways.

Both WDSC and VSG implement a different version of FPMD called Car–Parrinello molecular dynamics (CPMD; Car and Parrinello, 1985; Marx and Hutter, 2009). In contrast to Born–Oppenheimer ‘clamped nuclei’ molecular dynamics, the Car–Parrinello scheme explicitly involves solution of a system of coupled equations of motion for both nuclei and electrons: explicit electronic minimization at each time step, as in BOMD, is not needed since electron dynamics are followed in conjunction with the nuclei in time. After an initial electronic minimization, the fictitious dynamics of the electrons keeps them at the ground state corresponding to each new ion (nuclei) configuration. Ionic forces may be determined for each configuration. The fictitious mass of the electrons is chosen small enough to avoid a significant energy transfer from ionic to electronic degrees of freedom, hence to enforce adiabaticity. The small fictitious electron mass requires that the equations of motion

be integrated using a smaller time step compared to BOMD. WDSC and VSG both implement CPMD using DFT in the GGA. In GGA, the undesirable over binding effects of LDA are reduced. Neither WDSC nor VSG apply an empirical ‘pressure shift’ correction. A small degree of *under binding* is typical of GGA, however, the number of atoms, plane wave energy cut-off, time step and total run duration for the CPMD simulations of WDSC and (VSG) are 80 (100), 410 eV (950 eV), 0.3 fs (0.05 fs) and 10 ps (5 ps). FPMD of either type (BOMD or CPMD) are computationally taxing and this limits practical calculations to systems of order 100 atoms followed for 3–8 ps, generally at the lower end of the range. Calculation of shear viscosity from linear response theory requires longer runs that are computationally quite expensive. An example of such a calculation for viscosity of MgSiO₃ has recently been given by Karki and Stixrude (2010). Material properties that depend on particle statistics or long run durations such as self-diffusivity, shear viscosity, and glass dynamics are less precisely determined in short runs with small numbers of particles. Below we compare results of computed properties of liquid MgSiO₃ from these different FPMD studies at the same or similar state points to illustrate typical differences that can arise in property values.

An alternative to FPMD is the ‘classical’ molecular dynamics approach, EPMD. In EPMD, an empirical potential describing the (potential) energy between all atom pairs is used to compute forces. This effective pairwise-additive potential is derived a priori and is not part of the MD simulation per se. Because the electronic structure is not computed directly, systems with large numbers of particles (10⁴–10⁶) can be computed for long durations (1–10 ns) routinely. Potentials are generally developed using experimental data such as volume, compressibility, heat capacity, etc. to fix the potential parameters. Hybrid methods in which use is made of DFT calculations that are then parameterized to give effective pair potentials can also be used. Effective potentials include Coulombic, Born and van der Waals energy terms for all ion pairs. Fractional rather than integer charges are often used for the ions which improves the potential over purely ‘ionic’ models based on integer (valence) charge. The ability to perform EPMD simulations at many state points means that macroscopic equations of state (EOS) based on the MD results are precise for a given potential. This feature facilitates comparison of simulation and laboratory results that generally are quite spotty in PVT. Although empirical potentials can include three-body terms, the justification comes back to fitting experimental data and is not fundamental, in principle. The fundamental limitation of EPMD is that empirical or semi-empirical methods are required to determine effective pair potentials. Despite these limitations, carefully constructed transferable empirical potentials applicable for multicomponent silicates can make useful systematic geological approximations over relatively large ranges of *P* and *T*, as noted below.

The remainder of this paper is organized as follows. In the next section, the methods and results of EPMD calculations using the OG and M potentials are presented. Comparisons are made for the EOS, coordination statistics, self-diffusivities and shear viscosities over PT space. These

results are then compared to the EPMD results of BD and LRO and the FPMD results from SK, WDP and VSG as well as laboratory results. A final section summarizes what has been learned and steps for future work. A table of the many acronyms and abbreviations used in this paper for the sake of economy is provided in [Electronic Appendix -1 \(EA-1\)](#).

3. EPMD CALCULATIONS

In this section, a brief summary of the MD calculations is presented followed by a presentation of results for EPMD calculations for MgSiO₃ using the OG and M potentials. We will refer to the liquid simulated using the Matsui potential as the ‘M liquid’ and that based on the Oganov potential as the ‘OG liquid’ for brevity. A full description of the code and methods are presented elsewhere (Nevins, 2009; Spera et al., 2009). Results using identical methods for molten NaCl, Mg₂SiO₄, MgSiO₃ and CaAl₂Si₂O₈ are available elsewhere (Nevins and Spera, 2007; Ghiorso et al., 2009; Martin et al., 2009; Nevins et al., 2009; Spera et al., 2009) where more technical but standard details of the methods may be found.

3.1. Potentials

The M potential is a transferable potential derived for compositions in the system Na₂O–CaO–MgO–Al₂O₃–SiO₂. This potential was devised using experimental molar volume and compressibility data for 27 natural silicate phases to set the parameters of the pair potentials. The potential from OG was derived specifically for MgSiO₃ composition and is based on DFT calculations and semi-empirical methods utilizing ionization potential, electron affinity and other chemical properties for O, Mg and Si. The Buckingham form for the potential energy between two atoms *i* and *j* for both the M and OG potentials is:

$$V(r_{ij}) = \frac{q_i q_j e^2}{4\pi\epsilon_0 r_{ij}} + A_{ij} \exp\left(-\frac{r_{ij}}{B_{ij}}\right) - \frac{C_{ij}}{r_{ij}^6} \quad (1)$$

where q_i, q_j are the effective charges of species *i* and *j*, r_{ij} is the distance between the pair *ij*, e is the charge of the electron (1.60218×10^{-19} C), ϵ_0 is the vacuum permittivity (8.8542×10^{-12} C² m⁻¹ J⁻¹), A_{ij} and C_{ij} are parameters for the pair *ij* describing repulsive and van der Waals attractive forces, respectively, and B_{ij} is an *e*-folding length characterizing the radially-symmetric decay of electron repulsive Born energy between atom pair *ij*. Values for the potential parameters used in the simulations are collected in [Table 1](#). The justifications, derivations and parameters of the LRO and BD potentials are given in the original references. The potential expression of LRO is identical to Eq. (1); the potential model of BD includes, in addition to the Buckingham form, a term accounting for bond ionicity for each atom pair *ij* via a Morse potential term (Hofer and Ferreria, 1966; Matsui, 1998).

3.2. Methods

The essence of the MD computation is to compute the vector sum of all forces acting on each particle. The force

Table 1

Parameters defining the potential of Eq. (1) used in the effective pair-potential MD simulations in this study for molten MgSiO₃.

Pair potential parameter	Oganov et al. (2000)	Matsui (1996)	Units
	$q_{\text{Si}} = +2.9043$	$q_{\text{Si}} = +1.89$	
	$q_{\text{O}} = -1.6049$	$q_{\text{O}} = -0.945$	
	$q_{\text{Mg}} = +1.9104$	$q_{\text{Mg}} = +0.945$	
$A_{\text{Si-Si}}$	0	8.863704×10^{10}	kJ/mol
$B_{\text{Si-Si}}$	0	4.600000×10^{-3}	nm
$C_{\text{Si-Si}}$	0	4.257630×10^{-2}	kJ nm ⁶ /mol
$A_{\text{Si-O}}$	1.097039×10^5	4.840101×10^6	kJ/mol
$B_{\text{Si-O}}$	0.02827	1.610000×10^{-2}	nm
$C_{\text{Si-O}}$	0	7.825226×10^{-2}	kJ nm ⁶ /mol
$A_{\text{Si-Mg}}$	0	6.214048×10^{11}	kJ/mol
$B_{\text{Si-Mg}}$	0	6.300000×10^{-3}	nm
$C_{\text{Si-Mg}}$	0	2.508805×10^{-2}	kJ nm ⁶ /mol
$A_{\text{Mg-Mg}}$	0	1.986688×10^{10}	kJ/mol
$B_{\text{Mg-Mg}}$	0	8.000000×10^{-3}	nm
$C_{\text{Mg-Mg}}$	0	1.478312×10^{-2}	kJ nm ⁶ /mol
A_{MgO}	1.004808×10^5	3.141607×10^6	kJ/mol
B_{MgO}	0.02866	0.00178	nm
C_{MgO}	0	4.611011×10^{-2}	kJ nm ⁶ /mol
$A_{\text{O-O}}$	1.952624×10^5	6.231357×10^5	kJ/mol
$B_{\text{O-O}}$	0.02674	0.02760	nm
$C_{\text{O-O}}$	3.189199×10^{-4}	0.1438223	kJ nm ⁶ /mol

calculation is broken into long-range and short-range contributions. The simulations are run in the microcanonical (NEV) ensemble for which the internal energy, number of atoms and volume (density) are fixed. In fact, N and V are fixed exactly and the drift of the internal energy away from a constant value is a measure of the quality of the computation. Energy is conserved to about one part in 10^5 during the production run simulations presented below. Newton's equations of motion are solved using a time step of 1 femtosecond (1 fs). Atom trajectories (position and velocity) of all particles are determined (50 picoseconds (ps) for self-diffusion and EOS runs and ~ 5 nanoseconds (ns) for shear viscosity) according to the sum of pair potential forces. Periodic boundary conditions are used with the minimum image convention. The short-range cut-off used in all production simulations is 0.8 nm. The Coulombic long-range calculation is done using a particle-particle Ewald mesh which scales computationally as $N \log N$ and hence allows large particle-number systems to be studied. The simulation is broken into a pre-production and production phase. Once thermal equilibrium is achieved, a production simulation of 50 ps is made at the specified density and target temperature. Each production run is verified for equilibrium by comparing the average temperature of the initial and the final 10 ps of the 50 ps production run which should be identical within σ_T , the one-sigma temperature fluctuation of the production simulation. Additional tests to insure ergodicity based on the mean square displacement for each atom type have been applied following the methods previously described (Spera et al., 2009). Fluctuations in T and P arise due to the finite number of particles (N) in the system. The magnitudes of the fluctuations in temperature (σ_T) and pressure (σ_P) vary as $N^{-1/2}$ where N is the total number of atoms used in the simulation (McQuarrie, 2000). There is, therefore, an inherent uncertainty in any

ensemble-averaged computed property (e.g., diffusivity, isochoric heat capacity, compressibility, shear viscosity) related to the fluctuations in state point PT coordinates. All EPMD simulations performed in this study are for 8000 atom systems ($N = 8000$); typical temperature and pressure fluctuations are $\sigma_T = \pm 30$ K and $\sigma_P = \pm 0.30$ GPa, respectively. Fluctuations for a 1000 or 500 particle simulation would be greater by factors of 2.8 (± 85 K, ± 0.85 GPa,) and 4 (± 120 K, ± 1.2 GPa), respectively, and introduce more ambiguity in equations of state and transport property parameterizations. This intrinsic uncertainty should be kept in mind when evaluating results from MD computations. For a given potential, the precision of the EOS and other material property values therefore depends on the number of atoms considered in the simulation since at fixed density the implied T and P are known with uncertainties of σ_T and σ_P , respectively.

4. RESULTS

4.1. Equation of state and thermodynamic properties

One hundred fifty-eight EPMD simulations (76 for the OG liquid and 82 for the M liquid) of equilibrium or metastable MgSiO₃ liquid have been carried out along 18 isochores spanning the density range 1900–5300 kg/m³. Because glass is a non-equilibrium material we avoid state points within the glass field; our interests are strictly on equilibrium or metastable liquids, in this study. Pressure and temperature span the range, -0.88 to 231 GPa and 2507–5121 K, respectively. In [Electronic Annex-1 \(EA-1\)](#) and [Electronic Annex-2 \(EA-2\)](#) primary results are tabulated. For each state point simulation, the mean simulation temperature (T), simulation temperature fluctuation (σ_T), mean simulation pressure (P), simulation pressure fluctuation

(σ_p), internal energy (E), kinetic energy (E_K), potential energy (E_P) and self-diffusivity for Mg, Si, and O are provided. These data are the primary information used to calibrate the EOS and compute Arrhenian self-diffusion parameters (activation energy, activation volume and pre-exponential constants).

Computed values of E_P versus $T^{3/5}$ are shown in Fig. 1 for the M and OG liquids. Color versions of all the figures in this paper are given in [Electronic Appendix-3 \(EA-3\)](#). The observed linear relationship for virtually all isochores indicates that the scaling hypothesis of Rosenfeld and Tarazona (1998, hereafter RT98)

$$E_P = a(V) + b(V)T^{3/5} \quad (2)$$

where $a(V)$ and $b(V)$ are unspecified functions of volume (V) is closely adhered to. The function $a(V)$ gives the Helmholtz free energy at 0 K. Adherence to RT98 scaling has been demonstrated for a number of silicate liquids, including molten SiO₂ (Saika-Voivod et al., 2000), Mg₂SiO₄ (Martin et al., 2009) and CaAl₂Si₂O₈ (Ghiorso et al., 2009), molten CaMgSi₂O₆ and 1-bar eutectic liquid in the system CaMgSi₂O₆-CaAl₂Si₂O₈ (Martin et al., 2009) and for FPMD results of SK for MgSiO₃ and De Koker (2010) for liquid CaAl₂Si₂O₈. Both the OG and M liquid are found to satisfy Eq. (2) along a given isochore to a

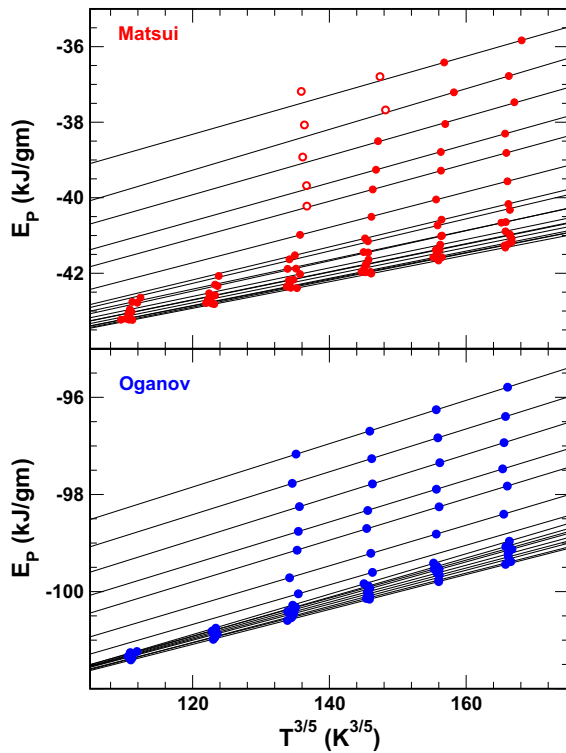


Fig. 1. Demonstration of RT-scaling (Rosenfeld and Tarazona, 1998) for the EPMD data sets computed using the Matsui (1996) potential (top) and the Oganov et al. (2000) potential (bottom). E_P is the potential energy and T is the temperature. Uncertainties are within the symbol size. The open circles represent state points deemed to lie below the computer glass transition (as construed from the computed self-diffusivity of O being $<10^{-10}$ m²/s) and were not included in constructing the RT EOS.

precision equivalent to the computed σ_T . Slopes and intercepts of the scaling relations are reported in Table 2. The functions $a(V)$ and $b(V)$ can be fitted from the linear parameterizations reported in Table 2 by utilizing techniques outlined in Ghiorso et al. (2009). Polynomial functions in specific volume are developed from these parameterizations and are reported in Table 3.

The molar internal energy, the sum of E_P and E_K where E_K is the kinetic energy associated with atomic vibration and mobility, is modeled by extending Eq. (2) as

$$E(V, T) = a(V) + b(V)T^{3/5} + \frac{3}{2}nRT \quad (3)$$

where the last term on the RHS is the classical high temperature limit of the molar kinetic energy for MgSiO₃ ($n = 5$). MD state point results for the OG and M liquid and the RT98 model results are compared in Fig. 2. The model provides excellent recovery of the data arrays. From Eq. (3), the isochoric heat capacity can be calculated:

$$C_V = \left(\frac{\partial E}{\partial T}\right)_V = \frac{3}{5} \frac{b(V)}{T^{2/5}} + \frac{3}{2}nR \quad (4)$$

and compared to the MD simulation values found by finite differencing of internal energies along isochores. This comparison is illustrated in Fig. 3. It should be noted that as $b(V)$ is always a positive quantity, the RT98 model expression for C_V implies a diminution of the heat capacity with increasing temperature to the asymptotic classical limit of $(3/2)nR$.

In Fig. 4, the ρ - P coordinates of all state points studied by MD simulation for the M and OG potentials are shown. As described in Martin et al. (2009) and Ghiorso et al. (2009), an equation of state and thermodynamic model for liquid MgSiO₃ can be developed from these data utilizing the RT98 scaling functions of Table 3 and a parameterization of V - P relations along a reference isotherm. Following our previous work, we employ the Universal EOS (Vinet et al., 1986),

$$P(T_o, V) = \frac{3K(1-x)e^{\eta(1-x)}}{x^2}, \quad \eta = \frac{3}{2}(K' - 1), \quad x = \left(\frac{V}{V_o}\right)^{1/3} \quad (5)$$

for the reference isotherm. The three parameters of this EOS, V_o , K and K' , are the zero pressure volume, isothermal bulk modulus, and the pressure derivative of the isothermal bulk modulus, for reference temperature T_o . Setting $T_o = 4000$ K, Universal EOS parameters are optimized from the data array and are reported in Table 4. A temperature-dependent equation of state (hereafter the RTU EOS),

$$P(V, T) = \left(\frac{T}{T_o} - 1\right) \frac{da(V)}{dV} + \frac{5}{2}T^{3/5} \left[\left(\frac{T}{T_o}\right)^{2/5} - 1 \right] \frac{db(V)}{dV} + \frac{T}{T_o}P(T_o, V) \quad (6)$$

is constructed from Eqs. (3) and (5) following Ghiorso et al. (2009). From the RTU EOS, all derivative and integral thermodynamic properties may be evaluated, and we will illustrate many of these model estimates in figures that

Table 2
Rosenfeld–Tarazona scaling ($U = a + bT^{3/5}$) for OG and M liquid MgSiO₃.

ρ (g/cm ³)	Matsui			Oganov		
	b (kJ/g K ^{3/5})	a (kJ/g)	R^2	b (kJ/g K ^{3/5})	a (kJ/g)	R^2
1.900	0.04270	-47.39	0.998263			
2.150	0.03885	-47.08	0.999930			
2.350	0.03773	-47.14	0.999943	0.04158	-105.87	0.999928
2.490	0.03701	-47.15	0.999951	0.04040	-105.77	0.999991
2.620	0.03663	-47.18	0.999957	0.03912	-105.65	0.999990
2.750	0.03605	-47.18	0.999980	0.03805	-105.55	0.999996
2.870	0.03582	-47.20	0.999986	0.03719	-105.46	0.999986
3.160	0.03517	-47.15	0.999996	0.03587	-105.36	0.999980
3.450	0.03534	-47.10	0.999975	0.03595	-105.40	0.999970
3.754	0.03712	-47.16	0.999891	0.03722	-105.52	a
4.010	0.03998	-47.27	0.999834	0.03910	-105.61	0.999982
4.240	0.04360	-47.41	0.999923	0.04076	-105.57	a
4.469	0.04690	-47.35	0.999891	0.04181	-105.32	0.999971
4.700	0.04949	-47.02	0.999970	0.04290	-104.95	0.999919
4.834	0.05059	-46.69	0.999870	0.04311	-104.60	0.999960
5.000	0.05167	-46.12	0.996511	0.04406	-104.23	0.999995
5.150	0.05392	-45.74	a	0.04415	-103.71	0.999985
5.300	0.05168	-44.52	a	0.04464	-103.20	0.999954

^a Fit based on two data points (see Fig. 1).

Table 3
Coefficients for Rosenfeld–Tarazona polynomial functions.

	$a(V) = \sum_{i=0}^6 c_i v^i$		$b(V) = \sum_{i=0}^6 c_i v^i$	
	Matsui liquid	Oganov liquid	Matsui liquid	Oganov liquid
c_0	323.437	127.116	-0.670324	-0.371466
c_1	-6507.31	-3503.98	16.4721	7.09542
c_2	46705.6	20724.4	-140.617	-45.7362
c_3	-175,474	-60212.0	593.293	139.020
c_4	364,151	86060.5	-1337.18	-201.487
c_5	-395,989	-48520.4	1546.78	112.513
c_6	176,383		-722.930	

follow. The smooth curves plotted in Fig. 4 are model predictions and illustrate the excellent applicability of the RTU EOS formalism to the OG and M liquid derived state point arrays.

The locus of points in P–T space along an isochore gives a measure of the “thermal pressure coefficient,” defined as

$$\left(\frac{\partial P}{\partial T}\right)_V = \frac{\alpha}{\beta} = \alpha K \quad (7)$$

where α is the isobaric expansivity, $\alpha(P, T) = \rho^{-1}(\frac{\partial \rho}{\partial T})_P$ and β is the isothermal compressibility, $\beta(P, T) = -\rho^{-1}(\frac{\partial \rho}{\partial P})_T$ or equivalently the inverse of the isothermal bulk modulus (K). Differentiation of Eq. (6) gives an RTU model expression,

$$\alpha K = \left(\frac{\partial P}{\partial T}\right)_V = \frac{1}{T_o} \frac{da(V)}{dV} + \frac{3}{2} T^{-2/5} \left[\frac{5}{3} \left(\frac{T}{T_o}\right)^{2/5} - 1 \right] \frac{db(V)}{dV} + \frac{P(T_o, V)}{T_o} \quad (8)$$

for the thermal pressure coefficient. In Fig. 5 we plot estimates of the thermal pressure coefficient obtained by finite differencing state points along isochores and compare these

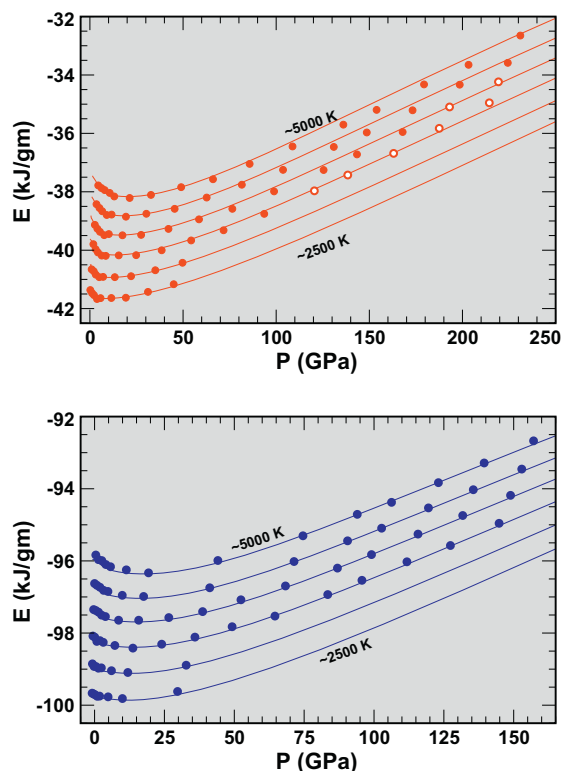


Fig. 2. Recovery of internal energy (E) for the Matsui (1996) potential (top) and Oganov et al. (2000) potential (bottom) EPMD data sets using the RT EOS model developed in the text. Uncertainties are within the symbol size. Open circles are defined in the legend of Fig. 1.

to model estimates. The RTU EOS evidently provides an excellent representation across the wide P–T range of the simulations except at the very highest pressures of the M

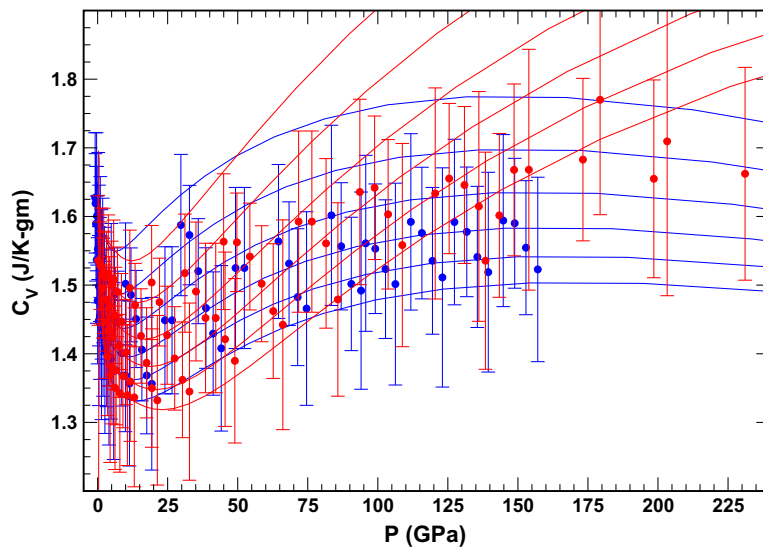


Fig. 3. Recovery of isochoric heat capacity (C_V) for the Matsui (1996) potential (red) and Oganov et al. (2000) potential (blue) EPMD data sets using the RT EOS model developed in the text. Data points are finite difference estimates from the state point arrays and uncertainties are calculated from error propagation techniques assuming uncorrelated variables. Isotherms are spaced at 500 K intervals over the range 2500–5000 K. (For interpretation of the references to color in this figure legend, the reader is referred to the web version of this article.)

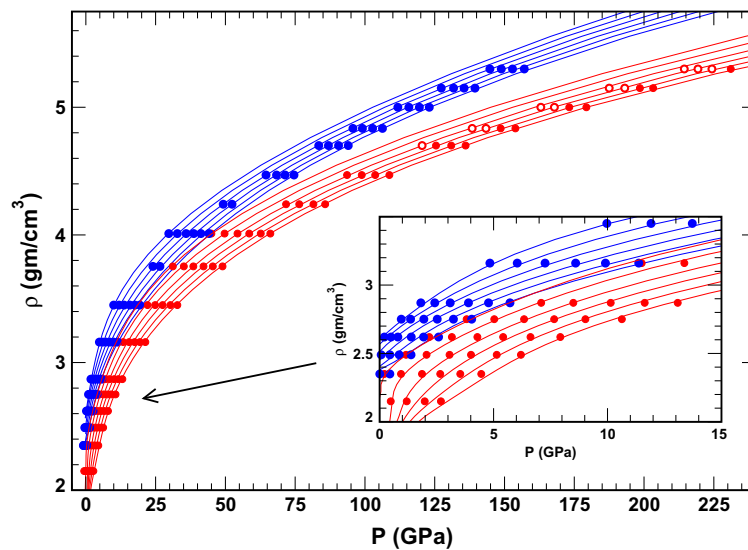


Fig. 4. Recovery of density (ρ) for the Matsui (1996) potential (red) and Oganov et al. (2000) potential (blue) EPMD data sets using the RT EOS model developed in the text. Uncertainties are within the state point symbols. Inset reveals the low-pressure region. Open circles are defined in the legend of Fig. 1. Isotherms are spaced at 500 K intervals over the range 2500–5000 K. (For interpretation of the references to color in this figure legend, the reader is referred to the web version of this article.)

Table 4
Universal EOS parameterizations of MD data along a nominal 4000 K isotherm.

	Oganov 4038.1 ± 15.7 K	Matsui 4049.2 ± 45.2 K
V_0	0.408031	0.815634
K	13.6262	0.142324
K'	7.66573	11.7246

liquid array. The results plotted in Fig. 5 demonstrate an important generalization apparent despite the obvious differences associated with the two potentials: values of the thermal pressure coefficient (in the figure depicted as the spacing between model isotherms) are larger at higher pressure than in the low-pressure regime. This is principally due to the strong pressure dependence of the bulk modulus (Fig. 6), which increases by about a factor of 200 over the

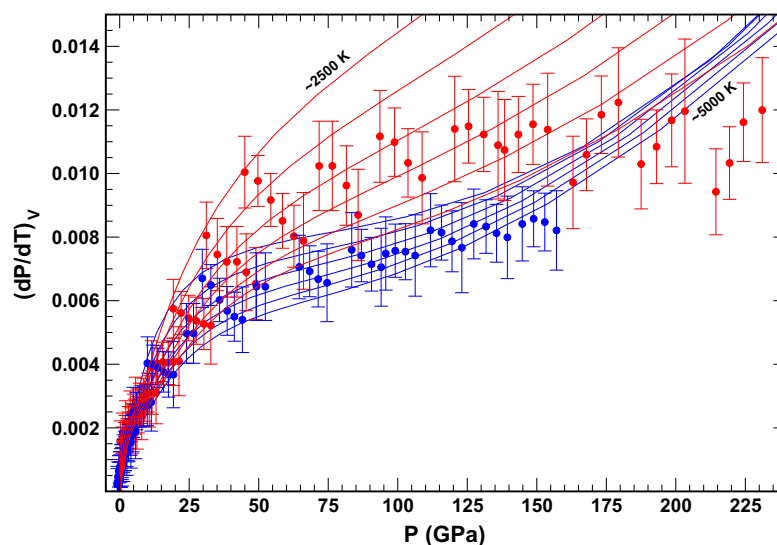


Fig. 5. Recovery of the thermal pressure coefficient $(dP/dT)_V$ for the Matsui (1996) potential (red) and Oganov et al. (2000) potential (blue) EPMD data sets using the RT EOS model developed in the text. Data points are finite difference estimates from state point isochore arrays and uncertainties are calculated from error propagation techniques assuming uncorrelated variables. Isotherms are spaced at 500 K intervals. (For interpretation of the references to color in this figure legend, the reader is referred to the web version of this article.)

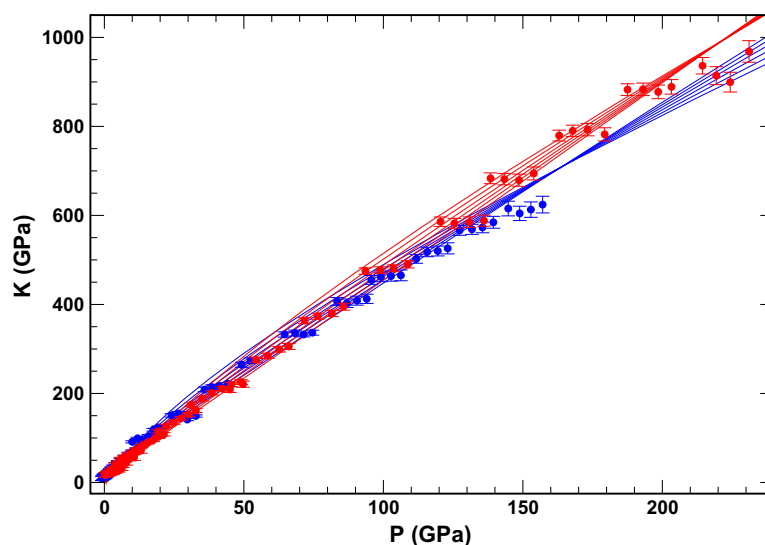


Fig. 6. Recovery of the bulk modulus (K) for the Matsui (1996) potential (red) and Oganov et al. (2000) potential (blue) EPMD data sets using the RT EOS model developed in the text. Data points are finite difference estimates from state point arrays and uncertainties are calculated from error propagation techniques assuming uncorrelated variables. Isotherms are spaced at 500 K intervals over the range 2500–5000 K. (For interpretation of the references to color in this figure legend, the reader is referred to the web version of this article.)

pressure range examined, as contrasted to the isothermal expansivity (Fig. 7), which diminishes over the same interval by about a factor of four.

Finally, we illustrate in Fig. 8 the pressure variation of the thermal Grüneisen parameter,

$$\gamma = \frac{\alpha KV}{C_V} \quad (9)$$

which varies from ~ 0.25 at zero pressure to a constant value of ~ 1 at high-pressure for the OG liquid and ~ 1.5 for the M liquid. It is significant that the thermal Grüneisen

parameter displays little dependence on temperature for either potential. We will return to this issue in a subsequent section of this paper.

4.1.1. Comparison of computational and laboratory data for liquid $MgSiO_3$

Model isotherms summarizing fits to the OG and M MD simulations are plotted in Fig. 9 along with other estimates of melt density obtained from previous MD studies and from laboratory experiments. The MD studies by BD and LRO are based on empirical force field potentials (EPMD).

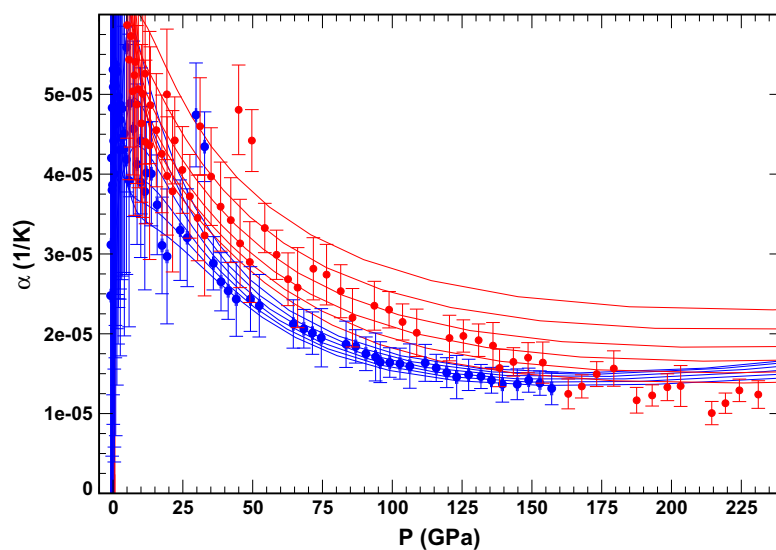


Fig. 7. Recovery of the isobaric coefficient of thermal expansion (α) for the Matsui (1996) potential (red) and Oganov et al. (2000) potential (blue) EPMD data sets using the RT EOS model developed in the text. Data points are finite difference estimates from state point arrays and uncertainties are calculated from error propagation techniques assuming uncorrelated variables. Isotherms are spaced at 500 K intervals over the range 2500–5000 K. (For interpretation of the references to color in this figure legend, the reader is referred to the web version of this article.)

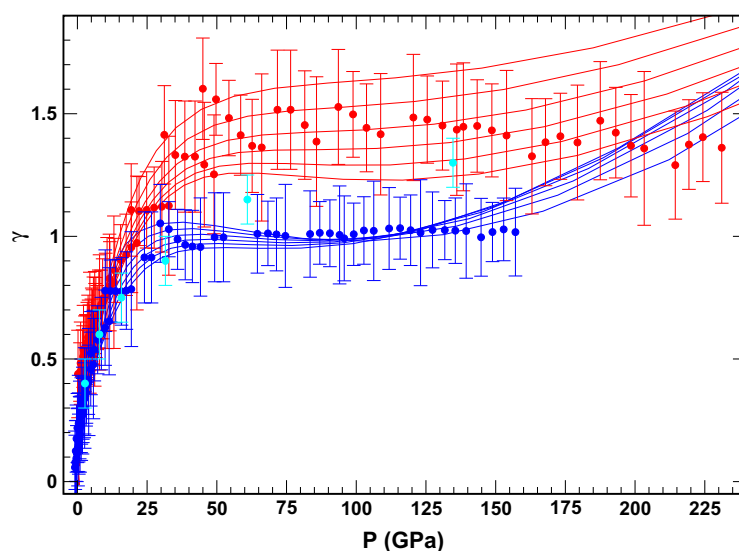


Fig. 8. Recovery of the thermal Grüneisen parameter (γ) for the Matsui (1996) potential (red) and Oganov et al. (2000) potential (blue) EPMD data sets using the RT EOS model developed in the text. Data points are finite difference estimates from state point arrays and uncertainties are calculated from error propagation techniques assuming uncorrelated variables. Isotherms are spaced at 500 K intervals over the range 2500–5000 K. For comparison, estimates of the Grüneisen parameter derived by Stixrude and Karki (2005) with uncertainties are shown in cyan. (For interpretation of the references to color in this figure legend, the reader is referred to the web version of this article.)

LRO report liquid densities, atomic self-diffusivities, and viscosities for eight state points at 3000 K. BD do not report MD simulation data for specific state points, but parameterize their results using a third-order Birch Murnaghan EOS. We plot three isotherms calculated from their parameterization. The Born–Oppenheimer FPMD study by SK provides 18 density–pressure state points along three isotherms (3000, 4000, and 6000 K) up to ~ 150 GPa. These authors make a

‘pressure shift’ empirical correction to computed results by fixing the density of the liquid at 1830 K to coincide with a laboratory-based estimate of melt density extrapolated from the model of Lange and Carmichael (1987). They also provide estimates of the Grüneisen parameter and liquid enthalpy over the same T–P range. WDSC report liquid densities for six state points along a 3500 K isotherm (88–135 GPa), and density, bulk diffusivity, and viscosity

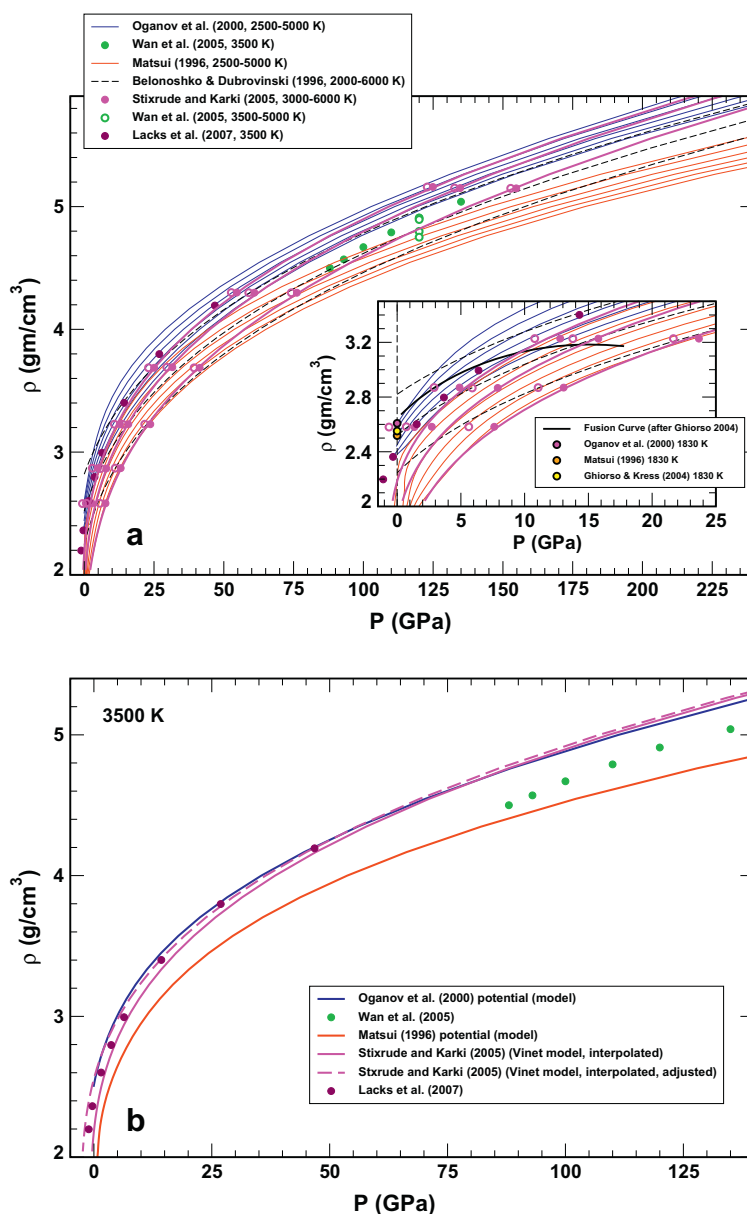


Fig. 9. Comparison of density (ρ) estimates from various FP and EPMD studies. (a) The curves plotted for the Oganov et al. (2000) and Matsui (1996) potentials are RT EOS parameterizations from this study. The Belonoshko and Dubrovinski (1996) curves are calculated from their reported EOS. The magenta curves passing through the Stixrude and Karki (2005) state points are obtained by fitting a Universal EOS (Vinnet et al., 1986) along each isotherm, independently. The open magenta symbols represent the Stixrude and Karki (2005) state points with their empirical 2 GPa pressure adjustment removed so that only the Pulay correction is applied to the “raw” FP ρ - P results; the empirical correction is applied so as to artificially bring the MD results into alignment with experimental data at low-pressure. (a) Inset shows the low-pressure region expanded with three estimates of the density at 1830 K and 1 bar indicated; the Ghiorso and Kress (2004) value and “Fusion curve” array are based on physical measurements. (b) Detailed comparison of data and model estimates at 3500 K. The interpolation for Stixrude and Karki (2005) is done by averaging our 3000 and 4000 K Vinnet fits to their state points. The dashed curve is shifted 2 GPa to remove the empirical correction as described in (a) (see text). (For interpretation of the references to color in this figure legend, the reader is referred to the web version of this article.)

for four state points (3500–5000 K) along a 120 GPa isobar from Car-Parrinello FPMD and have not been adjusted by application of an empirical ‘pressure correction’.

The densities of SK largely coincide ($\sim 2\%$ level) with the M-derived EPMD results at pressures below 50 GPa. At higher pressures their lower temperature densities are more

in accord with the results obtained from the OG potential, although the implied thermal pressure coefficient from the densest isochore of SK is at least a factor of three larger than that inferred from OG. The 3500 K isotherm of LRO essentially coincides with the 3000 K isotherm of SK, whereas the 3500 K isotherm of WDSC is close to

the 6000 K isotherm of SK. The discrepancy may owe its origin to the different methods used to approximate the exchange–correlation functional: GGA was used by WDSC whereas SK made the local density approximation. SK also made a correction to compensate for the over binding implicit in use of the LDA. Neither of these pressure corrections (empirical or Pulay) was made by WDSC. The sum magnitude of the corrections made by SK varies from 4 to 7 GPa depending on pressure. At 3500 K, the difference in calculated pressure at a density of 4600 kg/m³ between SK and WDSC is ~12 GPa, a factor of 2–3 times bigger than the corrections. The model isotherms calculated from BD do not extrapolate to zero pressure in a manner similar to any other study on MgSiO₃ liquid. Both the bulk modulus (inverse slope of the isotherms) and the thermal pressure coefficient (spacing of the isotherms) are larger than expected.

At zero pressure the MD results can be compared to estimates of the density of MgSiO₃ liquid obtained from laboratory experiments. While there are no direct experimental measurements on this liquid, densities can be calculated from the interpolative scheme of Ghiorso and Kress (2004). Results at 1830 K (the fusion temperature of enstatite as extrapolated to zero pressure) are compared in the inset of Fig. 9a to model estimates from M and OG liquids. The agreement is within 1% of the value of M and 2% of that of OG. The density of MgSiO₃ glass has been estimated at room temperature from Brillouin scattering measurements by Sanchez-Valle and Bass (2010). They obtain a value of 2.75 g/cm³ at ambient pressure and a maximal value of 3.5 g/cm³ at ~33.5 GPa. The former is broadly consistent with the liquid values (both experimental and MD) while the latter is significantly lower than any of the liquid estimates. One explanation for this discrepancy is that the compression of the glass does not permit the collapse and reorientation of long-range structures as likely occurs in the liquid state, thereby making the glass significantly less compressible at high-pressure when contrasted to the liquid. This is consistent with the general observation that glass, a frozen liquid, generally shares the vibrational and compressional properties of its corresponding crystalline polymorph and not that of the liquid. Ghiorso (2004) has estimated the density of MgSiO₃ liquid from analysis of the enstatite fusion curve. These estimates are plotted as the heavy solid curve in Fig 9a (inset), with intercept at zero pressure of 1830 K. The intercept value is about 5% higher than the number computed from Ghiorso and Kress (2004) and 3% higher than the estimate from the OG potential. At ~5 GPa, the melting curve lies at ~2250 K and climbs to ~2500 K at 10 GPa. The last is consistent with the 2500 K isotherm modeled from the M potential and broadly consistent with the 3000 K isotherm obtained by SK. In Fig. 9b density *versus* pressure is plotted for all models at 3500 K to facilitate direct comparison. At low P models generally converge with the difference in calculated pressure at fixed density within a few GPa. As density increases, the models diverge somewhat. Agreement between the LRO and OG model is excellent to ~50 GPa. The FPMD model of SK generally falls between the EPMD OG and M liquids approaching more closely the OG liquid

as P increases. The FPMD studies of SK and WDSC overlap for P ∈ (88–125 GPa) at 3500 K. From Fig. 9b, the SK and WDSC predicted pressures at melt density of 4615 kg/m³ differ by 11 GPa. This pressure difference is larger than the difference, at the same density and T, between the EPMD OG liquid and the FPMD SK prediction (ΔP = 8 GPa) and about the same (ΔP = 13 GPa) as the pressure difference between the FPMD results of WDSC and the EPMD M liquid. The disagreement between the two FPMD studies is about the same as between the EPMD studies. The EPMD study of LRO and OG essentially give identical results in ρ–P coordinates, which may be coincidental.

Estimates of the Grüneisen parameter at 4000 K developed by SK are plotted and compared to M- and OG-derived potential results in Fig 8. At low-pressures there is excellent agreement between the FPMD and EPMD OG liquid whereas at higher pressures the values trend above unity and are more in accord with results obtained using the M potential.

The speed of sound (c) may be calculated for MgSiO₃ liquid from the identity (Ghiorso and Kress, 2004):

$$\frac{1}{c^2} = \frac{\rho}{K} - \frac{\rho T \alpha^2}{\rho C_V + K T \alpha^2} \quad (10)$$

Model estimates of sound speed are plotted in Fig 10 and compared to an extrapolated value from an empirical model (Ghiorso and Kress, 2004) calibrated on experimental measurements. The agreement is excellent for results derived from the OG potential and good for that of M. The very weak temperature dependence of the modeled sound speed at low (<30 GPa) pressure is worth noting as is the fact that the speed of sound increases dramatically with pressure following the behavior of the bulk modulus.

SK estimate the enthalpy of MgSiO₃ liquid at each of their reported state points; we plot these for the 4000 K isotherm in Fig. 11. The reported enthalpies are adjusted to have zero intercept at zero pressure so that the pressure dependence of the enthalpy may be compared to similarly adjusted model values derived from the M and OG liquids reported in this paper. The adjustment is necessary because the zero point internal energies deduced from FPMD and EPMD studies are not known absolutely and depend on the assumptions inherent to each method/potential. The model curves plotted in Fig. 11 are calculated from the thermodynamic identity $H = E + PV$. Agreement between the OG RT EOS model and the SK FPMD estimates is excellent.

4.1.2. Shock wave data and computational models

A stringent test of computational models for liquid MgSiO₃ is comparison with high compression shock wave data. Mosenfelder et al. (2009) gives a comprehensive analysis for the system MgSiO₃ utilizing both shock and static compression experimental data. They review 13 points on the liquid MgSiO₃ Hugoniot with starting materials of either enstatite crystals (3 shots), porous enstatite (1 shot), an oxide mix (2 shots) or MgSiO₃ glass (7 shots). Restricting attention to the seven points with glassy MgSiO₃ starting material, shock temperature has been measured

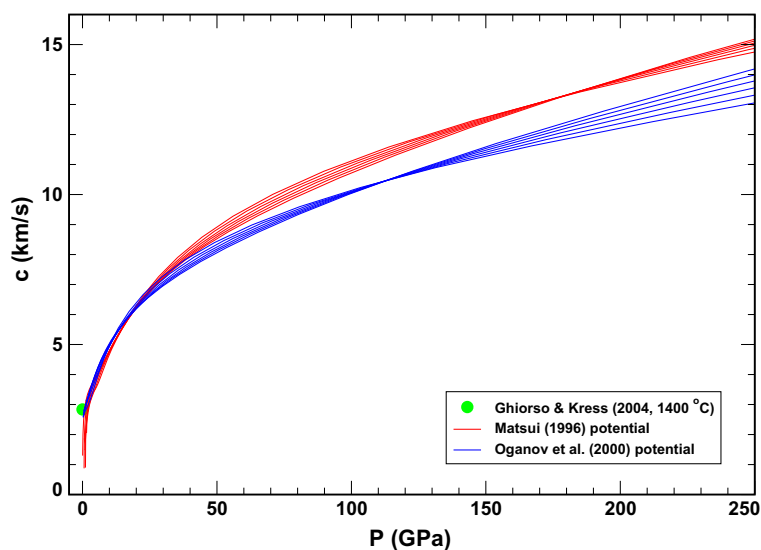


Fig. 10. Model estimates of bulk sound speed (c) calculated for the Oganov et al. (2000, blue) and Matsui (1996, red) potentials compared to a 1-bar estimate based upon physical experiments. Isotherms are spaced at 500 K intervals over the range 2500–5000 K. Note the very weak temperature dependence of the modeled sound speed, which is in agreement with physical measurements on silicate melts at low-pressure (Ghiorso and Kress, 2004). (For interpretation of the references to color in this figure legend, the reader is referred to the web version of this article.)

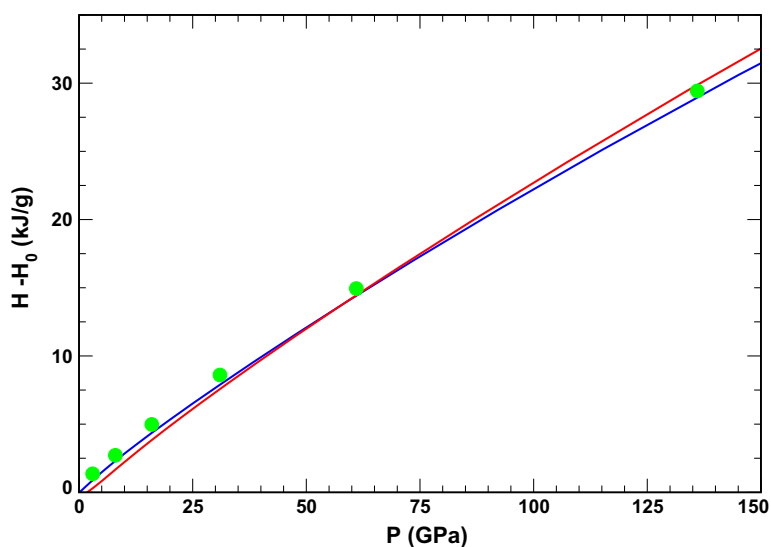


Fig. 11. Model estimates of enthalpy (H) relative to zero pressure at 4000 K for the Oganov et al. (2000, blue) and Matsui (1996, red) potentials compared to estimates along the same isotherm from the FP study of Stixrude and Karki (2005). (For interpretation of the references to color in this figure legend, the reader is referred to the web version of this article.)

for three shots (Akens et al., 2004; Luo et al., 2004). Measured shock temperatures, pressures and densities span the range $T \in (5000\text{--}6000\text{ K})$, $P \in (107\text{--}121\text{ GPa})$ and $\rho \in (4885\text{--}4978\text{ kg/m}^3)$, respectively. For the three cases where the shock temperature has been measured a comparison can be made to the EPMD predictions of the OG and M potentials and the Born–Oppenheimer FPMD estimates of SK. Results are shown in Fig. 12. Of all the models the OG liquid comes closest to matching the shock wave experiments, followed closely by SK, although at lower

pressures the M liquid seems to yield the better T – P – ρ estimates. Where the experimental data points are most secure (the glass starting material points with known shock temperatures) agreement with predictions based on the OG liquid is better than those from SK. This comparison suggests that results obtained from the OG EPMD simulations may give the best estimates of the density of MgSiO_3 liquid in the D'' region of the Earth's mantle. Unfortunately, due to the limited coverage in PT space of the FPMD simulations of WDSC and of VSG, construction

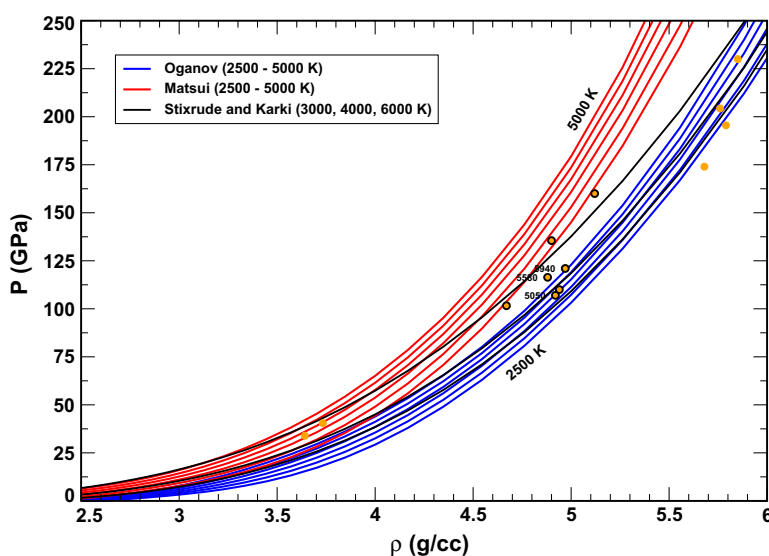


Fig. 12. Comparison of MD model estimates of density (ρ) to values inferred from shock wave studies (Mosenfelder et al., 2009, orange symbols); symbols outlined in black are data derived from shock melting of glass; other shock data represent shock melting of a crystalline solid. Temperatures (in K) of final shock conditions are indicated where reported. (For interpretation of the references to color in this figure legend, the reader is referred to the web version of this article.)

of the shock EOS based on CPMD is not possible. Shock wave data provide a very stringent test of theoretical equations of state and future modeling studies should pay particular attention to the shock data. Although we recognize the large computational costs of FPMD, every effort should be made to perform calculations at state points where experimental data exist. Otherwise, application of a computational model remains inchoate.

4.1.3. Summary of comparisons between proposed equations of state

A general conclusion drawn from the previous section is that the EPMD results derived from the OG potential come closest to estimating the density of MgSiO₃ liquid at the 1-bar melting point as inferred from the model of Ghiorso and Kress (2004) and from analysis of the T–P slope of the melting curve (Ghiorso, 2004). While the low-pressure P–T– ρ relations of SK correspond closely to the EPMD estimates derived from the M potential, SK performed an empirical shift of +2 GPa to pressure to make their densities correspond to estimates of the 1-bar value calculated from the model of Lange and Carmichael (1987). The unadjusted (i.e., raw) FPMD density estimates of SK imply a 1-bar density significantly higher than that suggested from either Lange and Carmichael (1987), Ghiorso and Kress (2004) or the melting curve analysis and is a manifestation of the over-binding implicit in LDA. At higher pressures, corresponding approximately to the base of the Earth's mantle, both the EPMD densities calculated from the OG potential and the FPMD estimates obtained by SK broadly match densities inferred from shock wave studies (Mosenfelder et al., 2009), with the OG potential yielding the better comparison. Results obtained from the M potential deviate markedly from all other studies above ~ 50 GPa, and this pressure should be taken as the limit of usefulness

of this parameterization. Overall, the OG potential appears to give the best results for simulating the density of MgSiO₃ liquid over the pressure–temperature range characterizing the Earth's mantle.

4.2. Structure of MgSiO₃ liquid

Nearest neighbor distributions encapsulate short- to medium-range order in a liquid and enable the connection between melt structure and properties to be rationalized. Short-range nearest neighbor structure is determined by statistical analysis of atom locations using partial pair correlation functions (radial distribution functions, RDF) expressed,

$$g_{ij}(r) = \frac{V}{N^2} \left\langle \sum_{i=1}^N \sum_{j=1, i \neq j}^N \delta(r - r_{ij}) \right\rangle \quad (11)$$

For atoms i and j , Eq (11) provides the normalized averaged distribution of atom j around a central i atom within a defined cut-off distance. V is the volume of the MD primary cell and N is the number of particles. The brackets denote averaging. Numerical integration of the RDF determines the coordination number for atom j around atom i based on locating the distance of the first minimum in the ij -pair RDF, $g_{ij}(r)$, following the first maximum. This cut-off distance is uniquely determined at each state point. Here, we focus on a subset of all nearest neighbor statistics, specifically Mg, Si and O around a central O and of O around central Si, and Mg atoms at 3000 and 5000 K. The notation $AB^{[n]}$ is used where n is the number of B atoms that are nearest neighbors to central atom A . For example, silicon octahedrally coordinated by oxygen is written SiO^[6] and oxygen coordinated to three nearest Si neighbors forming a tricluster is written OSi^[3].

4.2.1. Coordination statistics at 3000 K

In Fig. 13 coordination statistics at 3000 K are presented for the OG and M potentials. The color version of Fig. 13 in Electronic Appendix-3 (EA-3) makes structural comparisons easier to visualize and the reader is directed there. Fig. 13a depicts the CN of oxygen around Si. At zero

pressure both the OG and M liquids are dominated by 4-fold Si (90% for M and 70% for OG) that rapidly decreases as pressure increases. Pentahedral Si increases and reaches a maximum of 40% at 30 GPa for M and a maximum of 50% at 10 GPa for OG. The fraction of octahedrally coordinated Si increases monotonically for both M

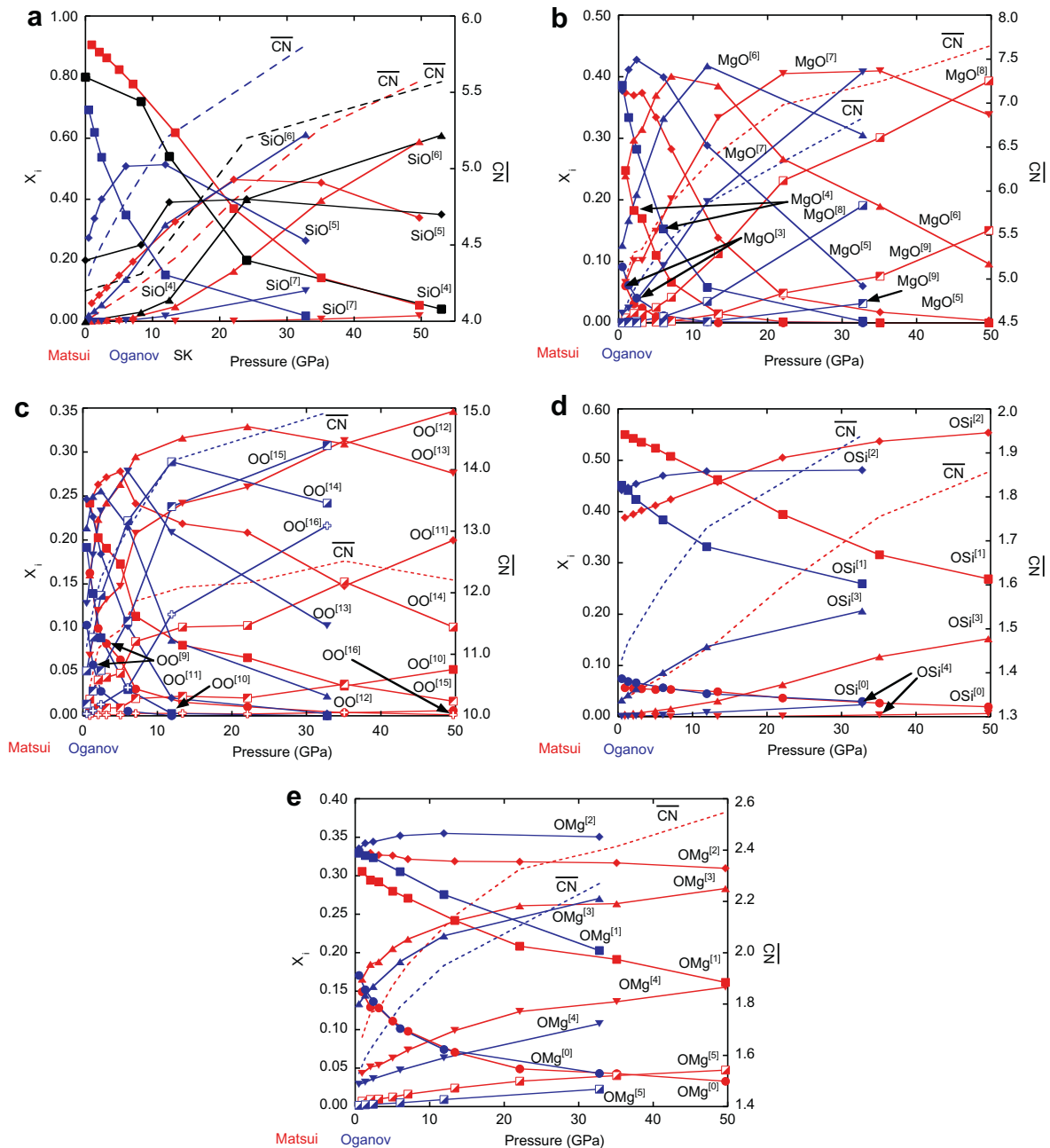


Fig. 13. Coordination statistics at 3000 K for the Matsui and Oganov potentials. (a) Coordination number of oxygen around central Si for the M and OG fluids. Squares show tetrahedral Si ($\text{SiO}^{[4]}$), diamonds show Si pentahedrally surrounded by oxygen ($\text{SiO}^{[5]}$), triangles show octahedral Si ($\text{SiO}^{[6]}$) and inverted triangles show 7-fold Si ($\text{SiO}^{[7]}$). Results from FPMD study (SK) plotted as X_i 's for 4-, 5- and 6-fold Si. Color version of this figure is in EA-2. (b) Coordination statistics for oxygen around Mg at 3000 K. (c) CN statistics for oxygen around oxygen at 3000 K. Following a rapid increase in the mean O around O coordination number ($\overline{\text{CN}}$), values flatten out for $P > \sim 15$ GPa. (d) Coordination statistics of Si around oxygen at 3000 K. The monotonic increase in $\overline{\text{CN}}$ is driven mainly by the decrease in non-bridging oxygen ($\text{OSi}^{[1]}$) and increase in tricluster oxygen ($\text{OSi}^{[3]}$). (e) CN statistics for Mg around oxygen at 3000 K. Note the rapid increase of $\overline{\text{CN}}$ at 0–15 GPa for both the M and OG fluid. Note the steep rise in tricluster oxygen between 1 bar and ~ 20 GPa for both the M and OG potentials.

and OG attaining 25% for M liquid and 50% of the total for OG liquid at 30 GPa. The main feature is that relative to M, the OG liquid exhibits a higher concentration of CN = 5 and CN = 6 species. That is, the mean coordination number of O around Si ($\overline{\text{CN}}$) at any pressure is higher for the OG liquid compared to M liquid as noted from the dashed curves representing the average coordination number in Fig. 13a. The coordination of oxygen around Mg is shown in Fig. 13b. The overall structure is similar to that of O around Si with an increasing abundance of higher coordination states with increasing pressure. $\overline{\text{CN}}$ of oxygen around central Mg is higher than the average coordination number of O around Si for both the M and OG potentials. $\overline{\text{CN}}$ varies from ~ 5 (distorted trigonal bipyramidal oxygen polyhedra) at low pressure to ~ 7.5 at 40 GPa. Structural changes to higher coordination states occur at slightly higher pressures for the OG *versus* M liquid unlike the behavior of O around Si where the order is reversed. The coordination environment of oxygen around oxygen is depicted in Fig. 13c. At all pressures the OG liquid shows a higher CN compared to the M liquid. The mean CN number increases rapidly for both M and OG from ~ 10 (for M) or ~ 11 (for OG) at zero pressure attaining values around 12 (M) or 14 (OG) around 10 GPa. For $P > 10$ GPa, $\overline{\text{CN}}$ levels off to around 12 (M liquid) or 15 (OG liquid).

In order to characterize melt polymerization mediated via metal–oxygen–metal connections it is useful to examine the coordination statistics of Si and Mg around central O atoms. In crystalline MgSiO₃, 66% of the oxygen has one nearest Si neighbor (i.e., OSi^[1]) and 33% of the oxygen is tetrahedral bridging oxygen (OSi^[2]) with two nearest neighbors of Si. Hence the mean coordination number of oxygen around Si is 4/3 in crystalline MgSiO₃ (enstatite and protoenstatite) at low pressure. In Fig. 13d, Si around O statistics are portrayed. At low pressure both OG and M are dominated by oxygen coordinated by one (55% for M, 45% for OG) or two (38% for M, 45% for OG) nearest neighbors of Si giving an average coordination number of 1.3 and 1.4 for the M and OG liquids. A small amount, $\sim 8\%$ of ‘free’ oxygen (OSi^[0]), that is oxygen with no nearest neighbor of Si, is also present. As pressure increases, the concentration of O with one nearest Si neighbor decreases whereas the concentration of 2-fold (bridging) and tricluster oxygen increases. The average coordination number shown on the right side of Fig. 13 increases from ~ 1.4 at low pressure for both M and OG to 1.7 (M) or 1.9 (OG) at 30 GPa indicating increasing extent of polymerization as pressure increases isothermally. Finally, the coordination of Mg around oxygen is shown in Fig. 13e. Both the M and OG liquid behave similarly with sub equal amounts ($\sim 35\%$) of oxygen with one or two Mg nearest neighbors and about 15% of tricluster oxygen (oxygen with three nearest neighbors of Mg) and ‘free’ oxygen (i.e., oxygen with no nearest neighbor of Mg) at low pressure. At 30 GPa, CN ~ 2.2 for OG and 2.4 for M exhibiting the increasing tendency towards polymerization as pressure increases.

4.2.2. Coordination statistics at 5000 K

For comparison with the coordination statistics at 3000 K, comparable statistics at 5000 K are presented in

Fig. 14. The pressure range of Fig. 14 is larger by a factor of three compared to the 3000 K results of Fig. 13 as dictated by the EOS. Differences in coordination statistics between 3000 and 5000 K are modest compared to the effects of pressure along an isotherm although there clearly are some differences. Average CN's at the same pressure for virtually all atoms are about 10–15% higher at 5000 K compared to 3000 K indicating a more ‘open’ structure as temperature increases isobarically (cf. Figs. 13a to 14a, 13b to 14b, 13d to 14d and 13e to 14e).

An especially interesting structural change is illustrated in Fig. 14c depicting the abundance of the oxygen–oxygen polyhedra (the oxygen ‘superlattice’) with pressure at 5000 K. The average CN of O around O (oxygen polyhedra) is ~ 10 (OG) and ~ 12 (M) at low pressure rapidly increasing and then flattening to ~ 15 (OG) or ~ 19 (M). At around 70 GPa the M liquid shows a rapid decrease in $\overline{\text{CN}}$ to ~ 12 . The OG liquid shows similar behavior with $\overline{\text{CN}}$ decreasing from ~ 15 to ~ 12 near 100 GPa. Evidently, the oxygen around oxygen mean coordination number is not a monotonically increasing function of pressure along an isotherm. At high pressure the oxygen superlattice assumes the form of an (irregular) icosahedron, OO^[12], a structure with an especially high packing efficiency (Tarnai and Gáspár, 1987; Clare and Kepert, 1991; Kottwitz, 1991). Both the OG and M liquids approach this asymptotic state of $\overline{\text{CN}} \sim 12$ at high pressure. Leech (1957) observed that the problem of maximizing the minimum distance between atoms is equivalent to the case of minimizing the repulsive potential energy (electron–electron hard core repulsion) of particles interacting pairwise with the repulsive potential energy varying as an inverse power of the inter-particle distance. This is equivalent to finding the polyhedron of equal sized spheres that maximizes the shortest polyhedra edge lengths. For $N = 2$ –12 and for $N = 24$ there are geometric proofs for the minimum energy configurations. Relatively high values of the packing density (ρ_p) are observed for the tetrahedron ($N = 4$, $\rho_p = 0.8453$), octahedron ($N = 6$, $\rho_p = 0.8787$), icosahedron ($N = 12$, $\rho_p = 0.8961$) and snub cube ($N = 24$, $\rho_p = 0.8617$). This is illustrated in Fig. 15 based on Table 10 in Clare and Kepert (1991). The icosahedron ($N = 12$) represents a global maximum packing density consistent with the minimization of the repulsive potential energy. Our conjecture is that the feature illustrated in Fig. 13c, the rapid decrease in the average coordination number of oxygen by oxygen, is driven by this energy minimization principle and represents a structural transition in response to high pressure. As pressure increases and bond distances decrease electron–electron repulsion between oxygen atoms dominates the energy landscape and repulsive energy minimization would naturally lead to the oxygen icosahedron (on average). It is significant that both potentials (OG and M) exhibit this structural change in the oxygen ‘superlattice’. As far as we know, sufficiently detailed and large particle number FPMD simulations on MgSiO₃ have not been carried out to test this conjecture and we know of no spectroscopic data that pertains. The other interesting feature of this structural transition is that it has no discernible effect on the P–T– ρ relations (e.g., Fig. 9), implying that there is little

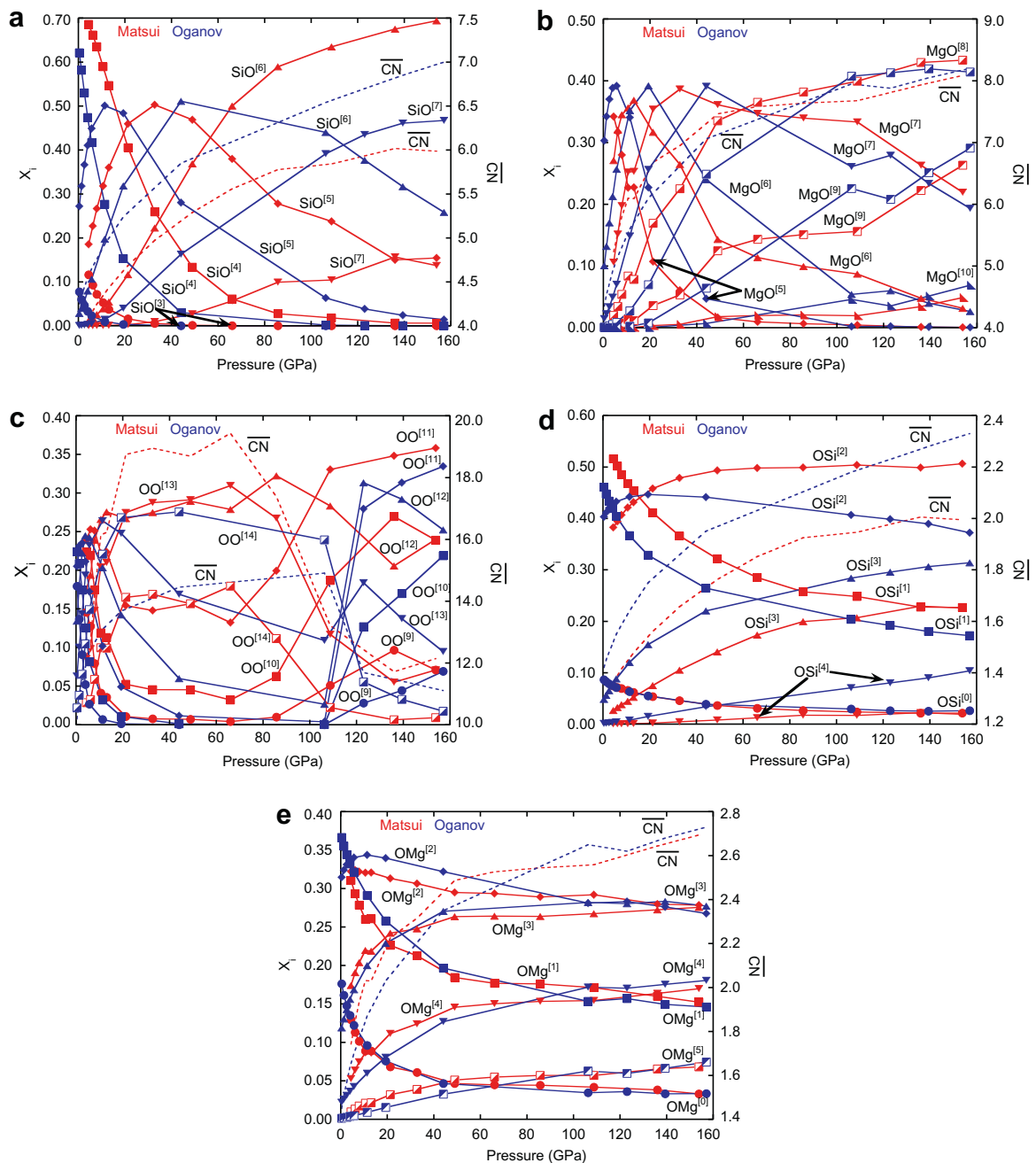


Fig. 14. Coordination statistics at 5000 K for the Matsui and Oganov potentials. (a) Coordination number of oxygen around central Si for the M and OG fluids. Squares show tetrahedral Si ($\text{SiO}^{[4]}$), diamonds show Si pentahedrally surrounded by oxygen ($\text{SiO}^{[5]}$), triangles show octahedral Si ($\text{SiO}^{[6]}$) and inverted triangles show 7-fold Si ($\text{SiO}^{[7]}$). A color version of this figure is in EA-2. (b) Coordination statistics for oxygen around Mg at 5000 K. (c) CN statistics for oxygen around oxygen at 5000 K. Following a rapid increase in the mean O around O coordination number ($\overline{\text{CN}}$), values flatten out for $P > \sim 25$ GPa. At ~ 80 GPa for the M fluid and ~ 100 GPa for the OG fluid there is a steep decline in $\overline{\text{CN}}$ that approaches the icosahedral global maximal packing efficiency state (see text). (d) Coordination statistics of Si around oxygen at 3000 K. The monotonic increase in $\overline{\text{CN}}$ is driven mainly by the decrease in non-bridging oxygen ($\text{OSi}^{[1]}$) and increase in tricluster oxygen ($\text{OSi}^{[3]}$). (e) CN statistics for Mg around oxygen at 3000 K. Note the rapid increase in $\overline{\text{CN}}$ in the range 0–15 GPa for both the M and OG fluid.

consequence of this transition expressed in the thermodynamic properties of MgSiO_3 liquid; by contrast, the transition does have an impact on transport properties as noted below.

4.2.3. Comparison with experimental and computational studies

Lee et al. (2008) have probed the local electronic structure of MgSiO_3 glass quenched from the liquid at 1923 K

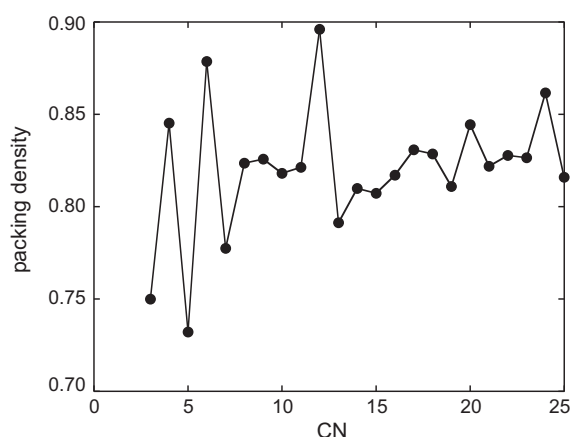


Fig. 15. Packing density *versus* coordination number for the packing of equal sized sphere around a common center (modified from Clare and Kepert (1991) Table 10). The local packing efficiencies for CN = 4 (tetrahedron), CN = 6 (octahedron) and N = 24 are noted. The icosahedron (a Platonic polyhedron) with CN = 12 represents a global maximum in packing efficiency, minimizing the electrostatic repulsive energy of the system. From Fig. 13c note that both the M and OG fluid approach the icosahedral packing of $\overline{\text{CN}} = 12$ for oxygen around a central oxygen.

by oxygen K-edge X-ray spectroscopy from 0 to 40 GPa. The pressure dependence of the spectral feature at 545 eV exhibits a marked step-wise change between 12 and 20 GPa. This feature is due, according to Lee et al., to an increasing abundance of tricluster oxygens (oxygen coordinated with three Si or OSi^[3]) as pressure increases although they could not quantify the magnitude of the effect in their study. It is nonetheless noteworthy because examination of Figs. 13d, 13e, 14d and 14e shows that there is a rapid increase in the sum of OSi^[3] and OMg^[3] (i.e., total tricluster oxygen) abundance as pressure increases. The tricluster sum abundance rises rapidly from small values at low pressure and approaches higher values ~ 20 GPa at 3000 K and ~ 40 GPa at 5000 K. Although a definitive quantitative comparison cannot be made, the EPMD results corroborate, at least qualitatively, the laboratory findings of Lee et al. (2008). Increasing tricluster oxygen has implications for the distribution of REE and other large ion incompatible elements because an increasing abundance of tricluster oxygen leads to a reduction in the free volume needed to host incompatible elements (e.g., Corgne et al., 2005) and may increase solid-liquid partitioning coefficients for large ion lithophile elements and the rare gasses usually considered incompatible with small solid-liquid partitioning coefficients in the mantle.

Recently, Wilding et al. (2010) determined the structure of MgSiO₃ liquid and glass at 1 bar using a novel levitation method and high-energy X-rays. They present experimental structure factor $S(Q)$ spectra for liquid MgSiO₃ at ~ 2300 K and 10^{-4} GPa (1 bar) and hence determine coordination number of O around Mg and O around Si. They find an average coordination number of O around Si of four identical to low-pressure results for the M liquid but somewhat

lower than $\overline{\text{CN}}$ of 4.2 for the more ‘disordered’ OG liquid. Wilding et al. (2010) also report an average coordination number for oxygen around Mg of $\sim 4.5 \pm 0.2$ at 2300 K in excellent agreement with our EPMD result of 4.6 for the M liquid and 4.5 for the OG liquid at 3000 K and 1 bar (Fig. 13b). For comparison, the EPMD results at 5000 K give a $\overline{\text{CN}}$ of O around Mg of ~ 4.2 for both the M and OG liquid. VSG report oxygen around Mg $\overline{\text{CN}}$ of 5.2 at 1 bar and 2200–2500 K based on CPMD. This is another example where the EPMD result agrees better with the experimental result than a FPMD calculation.

The coordination statistics for oxygen around Si at 3000 K and 0–50 GPa computed by FPMD (SK) can be compared to the M and OG liquid EPMD results. In making this comparison it is important to note that in the FPMD study 48 oxygen atoms were followed for 2.4 ps whereas in the EPMD results 4800 oxygen atoms were followed for 50 ps. Fig. 13a compares the O around Si statistics for the M and OG liquid to the FPMD study of SK. In general, the SK FPMD abundances of SiO^[4], SiO^[5] and SiO^[6] lie between those of the OG and M liquids perhaps being closer, on average, to the M liquid. For example, at 50 GPa, the concentrations of SiO^[4], SiO^[5] and SiO^[6] from FPMD are 4%, 35% and 61%, respectively, whereas for the M liquid the corresponding abundances are 4%, 34% and 58%, respectively (4% SiO^[7] is also present in the M liquid). All results, both FPMD and EPMD, show the same overall trends upon increasing pressure of monotonically decreasing tetrahedral Si, a concave down distribution of pentahedral Si that attains a maximum at some pressure (10 GPa for OG, 24 GPa for M, 26 GPa for SK) and monotonic increase of octahedrally coordinated Si such that at 50 GPa the abundance of octahedral Si is 75% for OG, 58% for M and 60% for SK. Given the very different methods and assumptions, the agreement between FPMD and EPMD predicted structures are reasonable. Without comprehensive spectroscopic data on the liquid it is impossible to know which local structure model is closest to reality.

Finally, we can make a comparison of the populations of bridging (OSi^[2]) and non-bridging (OSi^[1]) oxygen abundances at 1 bar between the CPMD calculation of VSG at 2273 K and $\rho = 2490$ kg/m³ with $N \sim 100$ atoms and the EPMD simulations for the M and OG liquids at 2500 K and $\rho = 2490$ kg/m³. The FPMD gives OSi^[1] = 65.5% and OSi^[2] = 34% whereas the M liquid gives OSi^[1] = 55% and OSi^[2] = 39% and the OG liquid gives OSi^[1] = 48% and OSi^[2] = 47%. Without experimental spectroscopic data it is difficult to come to any conclusion regarding relative accuracies.

4.3. Self-diffusivities of O, Mg and Si

The self-diffusivity of Mg, Si and O is related to the mean square displacement (MSD), a quantity computed directly from atom trajectories, by

$$D = \frac{1}{6N_{kt}} \left\langle \sum_{j=1}^{N_a} [r_j(t) - r_j(0)]^2 \right\rangle \quad (12)$$

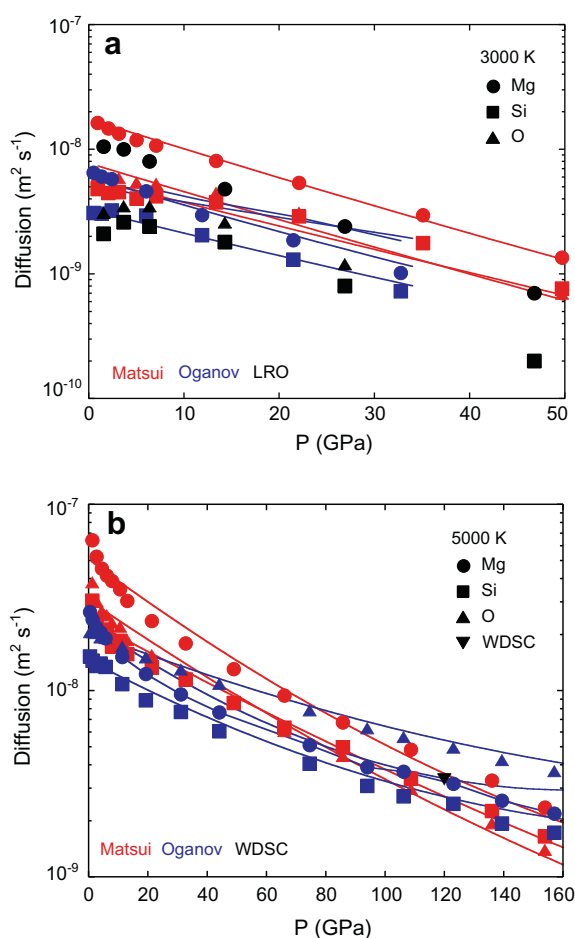


Fig. 16. Self-diffusion of Mg, O and Si in molten MgSiO_3 based on the Matsui (M) and OG potentials. Raw MD data as points; curves represent fits according to text Eq. (12). (a) Self-diffusion at 3000 K as a function of pressure. The M fluid is more mobile than the OG fluid. Results from the EPMD simulations of LRO are shown for comparison. Relative to the M fluid at 1 bar, the self-diffusivity of Mg is 1.3 and 2.6 times smaller, respectively, for the LRO and OG fluids. Self-diffusivities from OG and M at 3000 K agree to within a factor of 2.7 or less over the range of studied. Experimental diffusion data, which would allow us to distinguish the quality of the three EPMD potentials, do not exist. (b) Self-diffusion at 5000 K as a function of pressure. Agreement between OG and M self-diffusivities is somewhat better at 5000 K compared to 3000 K. At 120 GPa, for example, comparable diffusivities agree, at worst, to a factor of 1.8. In the pressure range 70–90 GPa there is considerable overlap in self-diffusivities.

where N_a refers to the number of atoms of species k and the quantity in brackets represents the MSD of the k th atom type. At each state point, the MSD for a particular atom is accumulated from the unfolded atom trajectories and a plot of MSD *versus* time is made. Following a brief (<50 fs) ballistic transport regime, the MSD becomes linear; the slope of the MSD is directly proportional to the self-diffusivity. Self-diffusivities for O, Si and Mg at all state points for the M and OG potentials are collected in the Electronic Annex for the M (EA-1) and OG (EA-2) potentials. Representative results are depicted at 3000 and 5000 K in Fig. 16

where D_k is plotted *versus* pressure. MD values are given as points; the curves are Arrhenian fits to the simulation results with activation volume a function of P and T according to, $v_A = v_{D_0} + v_{D_1}P + v_{D_2}T$. This form produces a superior fit compared to other Arrhenian forms (see Discussion in Spera et al., 2009). The self-diffusivity is a function of T and P according to

$$D = D_0 \exp\left(\frac{-[E_D + (v_{D_0} + v_{D_1}P + v_{D_2}T)P]}{RT}\right) \quad (13)$$

where D_0 , the frequency factor, is the diffusivity in the limit $T \rightarrow \infty$, E_D is the activation energy for diffusion, v_{D_0} , v_{D_1} and v_{D_2} constants describing the variation of the activation volume with P and T and R is the universal gas constant. Parameters for each species obtained from fitting the self-diffusivity values to Eq. (13) are given in Table 5. Except for Mg in the M liquid, all activation energies lie in the range 88–97 kJ/mol. Activation volumes at zero pressure and 0 K are all positive and, except for oxygen in the OG liquid, fall in the range 1.56–1.81 cm^3/mol . The variation of activation volume with P and T is very similar for all atoms for both the M and OG liquids. Increasing P and increasing T both lead to a decrease in the activation volume.

In Fig. 16 self-diffusivities for Mg, O and Si at 3000 K (Fig. 16a) and 5000 K (Fig. 16b) are depicted. In coordinates $\ln D$ *versus* P , a liquid with a constant activation volume yields a linear array, clearly not the case here. At 3000 K self-diffusivities of all atoms are faster for the M liquid compared to the OG liquid by factors of 2.6 (Mg), 1.6 (Si) and 1.4 (O). At 3000 K and pressure less than about 3 GPa, the effect of pressure is minimal. We do not observe a negative activation volume for either the OG or M liquid except for oxygen at 3000 K in the OG liquid. At 5000 K, atoms in the M liquid are again more mobile than in the OG liquid for $P < 20$ GPa. For $P > 20$ GPa, Mg and O are equally mobile (approximately) whereas oxygen becomes more mobile in the OG liquid. Activation volume for all atoms for both M and OG are strictly monotonically decreasing over the pressure range 0–160 GPa. Agreement between the OG and M liquid is better at 5000 K compared to 3000 K; the worst agreement between comparable values is a factor of 1.8. In most cases the agreement is better especially for $P \in (50\text{--}100)$ GPa. In summary, both the M and OG liquids exhibit similar self-diffusion characteristics with atomic mobility for all atoms greater in the M liquid at any pressure.

We are not aware of any laboratory values for Mg, Si or O self-diffusion in liquid or glassy MgSiO_3 with which to compare. We can however compare our results to both the FPMD results of WDC and the EPMD results of LRO at a few state points. WDC computed from FPMD a self-diffusivity of $3.33 \times 10^{-9} \text{ m}^2/\text{s}$ at 120 GPa and 5000 K valid for all atoms in liquid MgSiO_3 plotted as an inverted triangle in Fig 16b. In comparison, the MD values for O, Mg and Si for both potentials (M and OG) bracket the WDC result and fall between a maximum of $5.3 \times 10^{-9} \text{ m}^2/\text{s}$ (oxygen in OG liquid) and a minimum of $2.5 \times 10^{-9} \text{ m}^2/\text{s}$ (Si and oxygen in OG and M liquid). The agreement with the FPMD result of WDC is very good. Finally, we can compare our results

Table 5

Arrhenian fit parameters for atomic self-diffusivity of Mg, Si and O for the Matsui (M) and Oganov (OG) potentials. Arrhenian form is Eq. (13) in text.

Atom	D_0 (m ² /s)	E_D (kJ/mol)	v_{D_0} (cm ³ /mol)	v_{D_1} (cm ³ /mol GPa)	v_{D_2} (cm ³ /mol K)	R^2
<i>Matsui potential</i>						
Mg	2.60×10^{-7}	68.2	1.814	-1.794×10^{-3}	-1.346×10^{-4}	0.993
Si	2.11×10^{-7}	90.6	1.564	-6.356×10^{-4}	-1.446×10^{-4}	0.991
O	2.52×10^{-7}	88.0	1.795	-1.185×10^{-3}	-1.495×10^{-4}	0.992
<i>Oganov potential</i>						
Mg	1.90×10^{-7}	87.7	1.777	-3.259×10^{-3}	-1.418×10^{-4}	0.989
Si	1.47×10^{-7}	96.6	1.571	-1.857×10^{-3}	-1.511×10^{-4}	0.991
O	1.78×10^{-7}	90.2	1.017	-1.037×10^{-3}	-8.512×10^{-5}	0.993

with the EPMD results of LRO who computed self-diffusivities for Mg, Si and O at 3000 K and pressures in the range 1.5–47 GPa. The results from LRO at 3000 K, determined by EPMD are plotted in Fig. 16a. The LRO values are comparable to the M and OG results, especially at low pressure, although Si self-diffusion from LRO is everywhere smaller than either the M or OG liquid. This is probably due to the use of the BKS force field (van Beest et al., 1990) LRO. For $P > \sim 25$ GPa, self-diffusivities of all atoms are smaller by a factor of 3-compared to the values based on the OG and M potentials.

Based on these results, we conclude that to within a factor of ~ 2 , all EPMD results are consistent, especially for P less than ~ 20 GPa. Interestingly, LRO Mg self-diffusivities are closer to the analogous quantity in the M liquid whereas for both Si and oxygen LRO values compare more favorably to the OG liquid. Laboratory studies of Mg, O and Si self-diffusion at elevated T and P are needed for comparison to the broad range of results from extant MD studies in order to rank the performance of the computational models.

4.4. Shear viscosity

The shear viscosity is computed using Green–Kubo Linear Response Theory. Specifically, shear viscosity is determined by analyzing the temporal decay of the five independent components (both on and off-diagonal) of the stress tensor. A discussion of the details and implementation is provided by Nevins and Spera (2007). The Green–Kubo (GK) expression for the shear viscosity is found by integration of the stress (pressure) autocorrelation function. For example, for the off-diagonal stress components the expression is

$$\eta = \frac{V}{3kT} \int_0^\infty \left\langle \sum_{x < y} P_{xy}(t) P_{xy}(0) \right\rangle dt \quad (14)$$

where η is the shear viscosity, V is the system volume, k is Boltzmann's constant, and P_{xy} refers to the xy component of the stress. In addition to the off-diagonal components P_{xy} , P_{xz} and P_{yz} , two normal components ($P_{xx}-P_{yy}$) and ($P_{yy}-P_{zz}$) are also used to compute the shear viscosity from the raw MD results. The reported shear viscosity is the average of the five distinct values and its uncertainty is the standard deviation of these values. Computed values

of the shear viscosity in the range 3500–4500 K are shown in Fig. 17 as a function of pressure for the M and OG liquids. Each isotherm is labeled with the actual average simulation run temperature, which is generally quite close to the nominal values of 3500, 4000 and 4500 K, respectively. The simulation T fluctuations (one-sigma) are also given on the diagram. Points represent the MD values: circles for nominal 3500 K runs, squares for nominal 4000 K runs and triangle for a single nominal 4500 K simulation. The curves represent fits of the OG and M shear viscosities based on the modified Arrhenian relation,

$$\eta = \eta_0 \exp\left(\frac{E_\eta + (v_{\eta_0} + P v_{\eta_1})P}{RT}\right) \quad (15)$$

where E_η is the activation energy for viscous flow and the activation volume for viscous flow is a function of pressure

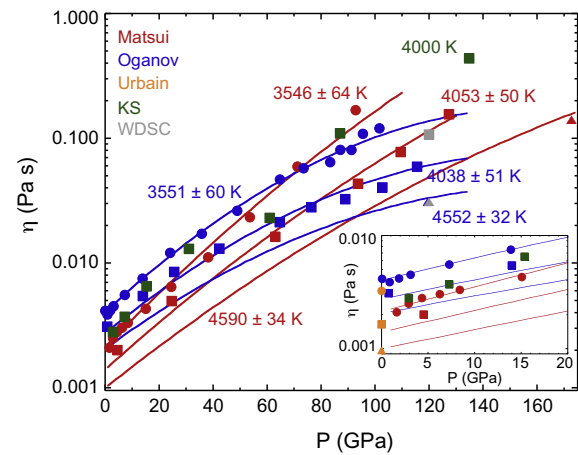


Fig. 17. Shear viscosity for liquid MgSiO₃ based on the Matsui and Oganov potentials for T at 3500–4500 K as a function of pressure. Points are raw EPMD data; curves are Arrhenian fit to raw data. Fit parameters are collected in Table 6. Two points at 120 GPa from the FPMD study of Wan et al. (2007) are shown in gray. The 4000 K WDSC value (Wan et al., 2007) is consistent with the Matsui potential whereas the 4500 K WDSC value lies along the Oganov 4500 K isotherm. Inset expands the low pressure and includes the experimental data from Urbain et al. (1982). Green squares show KS (Karki and Stixrude, 2010) FPMD results at 4000 K. (For interpretation of the references to color in this figure legend, the reader is referred to the web version of this article.)

Table 6

Arrhenian parameters for liquid MgSiO₃ shear viscosity for the Matsui (M) and Oganov (OG) potentials and for the FPMD results (19 viscosity values) of Karki and Stixrude (2010). Arrhenian form is Eq. (15) in text.

Potential or Source	η_0 (Pa s)	E_η (kJ/mol)	v_{η_0} (cm ³ /mol)	v_{η_1} (cm ³ /mol GPa)	R^2
Matsui	7.67×10^{-5}	97.9	1.509	-2.264×10^{-3}	0.998
Oganov	4.02×10^{-3}	95.1	1.375	-4.219×10^{-3}	0.993
Karki and Stixrude (2010)	1.34×10^{-4}	88.7	2.152	-6.967×10^{-3}	0.939

only, $V_\eta = v_{\eta_0} + Pv_{\eta_1}$. Calculated fit parameters are gathered in Table 6. Activation energy and volume are similar for the two potentials: $E_\eta = 98$ and 95 kJ/mol and $v_{\eta_1} = 1.51$ and 1.38 cm³/mol for the M and OG fluids, respectively. The main difference is in the pre-exponential term (η_0) such that the M liquid is less viscous than the OG liquid in the limit $T \rightarrow \infty$ at 0 pressure. This is consistent with the ordering of self-diffusivity between the OG and M liquids. However, the M liquid becomes stiffer than the OG liquid at higher P (70–90 GPa depending on T), a reflection of the greater activation volume of the M liquid. Differences in predicted shear viscosity between the two potentials are rather small, generally within a factor of 2 or less with the greatest divergence (not surprisingly) for $P > 100$ GPa. At 3500 K, the OG liquid exhibits a viscosity range from 4.1×10^{-3} Pa s at 1 bar to 0.12 Pa s at 100 GPa whereas the M liquid varies from 2.2×10^{-3} Pa s at 1 bar to 0.14 Pa s at 100 GPa. At the pressure of the core–mantle boundary on Earth, the estimated shear viscosity of liquid MgSiO₃ is 0.05 Pa s at 4000 K and 0.028 Pa s at 4500 K for the OG liquid. These can be compared to the zero pressure values of 0.0027 and 0.0022 Pa s at 4000 and 4500 K, respectively, for the OG liquid. These values imply a viscosity stratification of about a factor of 10–20 across a whole mantle Hadean magma ocean.

EPMD results are compared to FPMD results in Fig. 17. WDSC estimated shear viscosity at 120 GPa and 4000 and 4500 K based on their FPMD self-diffusivities and the Debye–Einstein–Stokes formula derived by Zwanzig (1983). These two points are plotted in Fig. 17. Rather interestingly, the WDSC point at 4000 K sits on the M 4000 K isotherm and their result at 4500 K lies on the OG liquid 4500 K isotherm. By any account, the agreement between the FPMD results of WDSC and the EPMD predictions is excellent. Recently, Karki and Stixrude (2010) presented results for shear viscosity based on Born–Oppenheimer FPMD for liquid MgSiO₃ along the 3000, 4000 and 6000 K isotherms for a range of pressures. The KS 4000 K data are shown as green squares in Fig. 17 (EA-3). In order to facilitate comparisons, viscosity values from Karki and Stixrude (2010) have been fit to the modified Arrhenian expression of Eq. (15). Fit parameters are given in Table 6. For P up to ~ 60 GPa, the KS values correspond very well to the OG liquid points except for one point at 31 GPa. However, the two highest pressure points from KS, at 82 GPa and 135 GPa, deviate from the OG liquid by factors of 2.8 and 7, respectively. In summary, we directly compare shear viscosities at the single state point $T = 4000$ K and $P = 120$ GPa for the OG liquid (0.06 Pa s), the FPMD result from WDSC (0.10 Pa s), the M liquid (also 0.10 Pa s) and the FPMD result of KS (0.3 Pa s). Thus, at this single

state point estimates of the shear viscosity vary by a factor of five. We note that there is closer conformity between the EPMD predictions of shear viscosity (M and OG) at 4000 K than between the two FPMD studies (WDSC and KS). Unfortunately, there are no experimental measurements of the shear viscosity of liquid MgSiO₃ at high pressure. That is, while models can be compared they cannot be tested against observation.

Finally, a comparison can be made between 1 bar experimental viscometric data from Urbain et al. (1982) and the ‘computer liquids’ provided the latter are extrapolated to lower temperature. In Fig. 18 viscosity at 1 bar pressure for molten MgSiO₃ for the M and OG liquids, the FPMD KS liquid and experimental values from Urbain et al. (1982) are plotted and compared. Although the raw MD results do not extend to low T and the Urbain et al. (1982) measurements are restricted to temperatures below 2270 K, this is the only direct comparison, however imperfect, that can be made between experiment and simulation. The zero pressure Arrhenian Fit parameters for the OG and M liquids, the FPMD values from KS and the laboratory data of Urbain et al. (1982) are given in Table 7. For the FPMD, the VTF viscosity at 1 bar used by Karki and

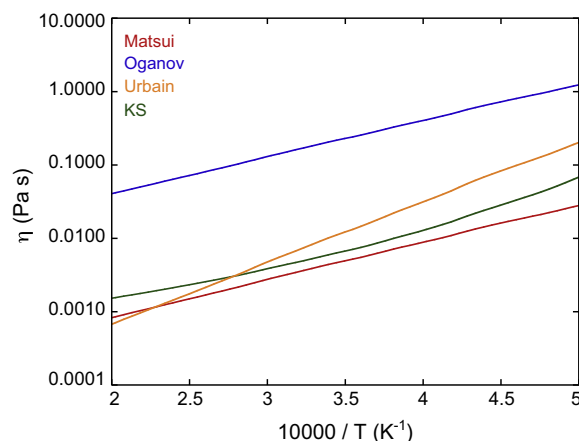


Fig. 18. Shear viscosity of liquid MgSiO₃ at 1 bar and temperatures between 2000 and 5000 K based on EPMD results for the M (red) and OG (blue) liquids and the FPMD (green) results from Karki and Stixrude (2010) compared to experimental results (orange) from Urbain et al. (1982). The experimental results have been extrapolated to higher T and the computer fluids have been extrapolated from ~ 3000 K to lower T . The activation energy for viscous flow (E_A) based on laboratory measurements is significantly higher than that of any computer liquid. (For interpretation of the references to color in this figure legend, the reader is referred to the web version of this article.)

Table 7

Arrhenian parameters for liquid MgSiO₃ at 1 bar (10⁻⁴ GPa) from models and experiments. Models include: EPMD results (M and OG liquid) and FPMD results (Karki and Stixrude, 2010). Laboratory results by concentric cylinder viscometry are from Urbain et al. (1982).

Model or data source	η_0 (Pa s)	E_η (kJ/mol)
EPMD (M liquid)	7.67×10^{-5}	97.9
EPMD (OG liquid)	4.02×10^{-3}	95.1
FPMD (KS)	1.38×10^{-4}	96.6
Experiment (Urbain et al.)	1.38×10^{-5}	158.8

Stixrude (2010), $\eta = 4.31 \times 10^{-4} \exp(5000/(T - 1000))$, is plotted in Fig. 18 rather than the Arrhenian fit based on their data. There are three main points to be drawn from examination of Fig. 18 and Table 7: (1) the three computational models give essentially identical values of the viscous flow activation energy of 96 ± 2 kJ/mol, (2) this value is considerably smaller than the experimental value of ~ 160 kJ/mol and (3) the FPMD KS and EPMD M models come closest to agreement. The factor of ~ 1.7 difference in E_η between experiment and models may be due to the relatively small range in T (1987–2268 K) and low mean T for which laboratory data are available. Specifically, experimental data were collected near 2000 K whereas the computer fluids were studied at $T > 3000$ K; it is known that the apparent energy of activation decreases as T increases, in general. In contrast, the model fluids are fit over a T range of ~ 3000 K. Alternatively, it could be that the models systematically underestimate E_η . More experimental studies of the shear viscosity of liquid MgSiO₃ especially at high pressure and temperature are needed.

5. CONCLUSIONS

MgSiO₃-rich perovskite, the most abundant mineral on Earth, makes up about 70% of the lower mantle. As a consequence, molten MgSiO₃ serves as a first approximation to the material of the Earth's Hadean magma ocean and of silicate liquid that may exist today along the core-mantle boundary defining an ultra-low velocity zone (e.g., Xu and Koper, 2009). Because of its planetary significance, it is important to quantify the thermodynamic, transport and atomic structure of molten MgSiO₃. Although there have been a number of experimental and computational studies of liquid MgSiO₃, there has not been a detailed comparative analysis between laboratory investigations (Raman scattering, high energy X-ray diffraction, fusion curve determination, shock wave EOS) and computational studies. The primary purpose of this study has been, therefore, to evaluate the consistency of extant computational models and to compare results to laboratory data. We have used both the transferable empirical pair potential of M and a pair-potential independently developed by OG to compute the thermodynamic and transport properties of MgSiO₃ liquid by MD simulation. Additional published work including two other EPMD studies and three FPMD studies have been compared and contrasted with respect to thermody-

amic, transport and structural properties whenever possible.

Comparisons of theoretical models for MgSiO₃ liquid are hampered by the lack of comprehensive coverage in P-T space of some studies. For example, a detailed comparison between the three FPMD studies cannot be made since coverage in P-T space barely overlaps. The VSG study reports information at only 1 bar and one temperature (~ 2350 K). Where the FPMD studies of SK and WDSC do overlap (e.g., at 3500 K for $P \in 88$ –125 GPa) there are quantitative differences, which may be related to the particular flavor of FPMD implemented. For example, the SK and WDSC predicted pressures at melt density 4615 kg/m³ differ by 11 GPa at 3500 K. This pressure difference is larger than the difference, at the same ρ and T , between the EPMD OG liquid and the FPMD SK prediction ($\Delta P = 8$ GPa). Similarly the pressure difference between the M liquid and the WDSC prediction (at the same density and T) is 13 GPa. At lower melt densities, agreement between all five models – the EPMD of LRO, M and OG and the FPMD model of SK – is better. At a density of 2600 kg/m³, a pressure difference of 4 GPa encompasses all models (at 3500 K). In comparing only the EPMD models, the LRO model and the OG model are nearly coincident (at 3500 K) over the range 0–50 GPa.

A stringent test of computational models for liquid MgSiO₃ is comparison with the shock wave data from Mosenfelder et al. (2009) especially in those cases where the shock temperature is measured and the starting material is appropriate. Restricting attention to three points on the Hugoniot with glassy (not liquid) MgSiO₃ starting material and for which the shock temperature has been measured a rough comparison can be made to the EPMD predictions. Of all the models the OG liquid comes closest to matching the shock wave experiments with densities in the range 4880–4970 kg/m³ and $T \in (5000$ –6000 K).

Comparison of model coordination statistics with high-pressure Raman spectroscopy and container-less high-energy X-rays is hindered by the lack of sufficient information presented in some of the modeling studies as well as possible differences between liquid and glass structures. For the two models with sufficient coordination statistics to make a valid comparison (the OG and M liquids studied here), agreement between experiment and predictions is quite good. A comprehensive study of in situ MgSiO₃ liquid at elevated pressures along a high-T isotherm would be most helpful in resolving differences in model predictions. Perhaps the most interesting aspect of the coordination statistics is the prediction of a decrease in the mean oxygen around oxygen CN around 70 GPa. This feature was found for both the OG and M liquid and is consistent with a global maximum of packing efficiency of oxygen around oxygen corresponding to icosahedral ($N = 12$) packing. We suggest that at high pressure, Born repulsion dominates over other forces and the icosahedral packing arrangement results because it is the one that minimizes repulsive forces. It would be interesting to conduct a large particle number FPMD study to test this conjecture. Spectroscopic high-pressure data would also be very useful in testing the icosahedral packing conjecture proposed here.

Unfortunately, there are no laboratory results for O, Mg or Si self-diffusion or for shear viscosity available at elevated T and P for liquid MgSiO₃. We can only compare the various models through overlapping portions of PT space. On the whole there is a general agreement to within a factor of three or better. Two comparable state points from the FPMD study of WDSC essentially match the EPMD results for shear viscosity. For self-diffusion the values of LRO generally fall between those from M and OG except for Si. At 5000 K, a point from WDSC is consistent with both the OG and M liquid. Once again, accurate experimental values of *D* and η at elevated PT are needed for comparison. For shear viscosity, the FP results of Karki and Stixrude (2010) generally lie above the EPMD results at 4000 K whereas two points from WDSC fall directly on the EPMD results at 4000 K and 120 GPa.

A primary conclusion of this study is that there is a desperate need for more laboratory measurements on liquid MgSiO₃. In particular measurements of the density of the liquid along a few isotherms as a function of pressure, of Mg, O and Si self-diffusivities and of shear viscosity would enable one to discriminate between computational models. Better control on the melting curves of MgSiO₃ polymorphs, especially in the range 20–60 GPa would be very helpful in constraining the liquid density. Spectroscopic studies allowing one to deduce O around O, Si around O, Mg around O and O around Si coordination statistics would be especially helpful. Without this information it is very difficult to access the accuracy of the various computational models. The final words on the properties of liquid MgSiO₃ have not been written.

ACKNOWLEDGMENTS

This research was supported by an allocation of advanced computing resources from the National Science Foundation and the Office of Science of the US Department of Energy. We acknowledge support from NSF Grants ATM-0425059, EAR-0838182, EAR-0440057 and DOE Grant DE-FG-03-91ER-14211 and the University of California Santa Barbara. Ian Cutler, Ben Martin and Brian Kelly aided in performing the computations. We thank L. Stixrude, J. Wan, and N. de Koker for sharing data and discussion. This is OFM Research contribution #16 and UCSB Earth Research Institute contribution 10-452. We also thank two anonymous reviewers as well as AE Mike Toplis for valuable comments.

APPENDIX A. SUPPLEMENTARY DATA

Supplementary data associated with this article can be found, in the online version, at doi:10.1016/j.gca.2010.12.004.

REFERENCES

- Akins J. A., Luo S. -N., Asimow P. D. and Ahrens T. J. (2004) Shock-induced melting of MgSiO₃ perovskite and implications for melts in Earth's lowermost mantle. *Geophys. Res. Lett.* **31**, L14612.
- Alfe D., Price G. D. and Gillan M. J. (2002) Iron under Earth's core conditions: liquid-state thermodynamics and high-pressure melting curve from ab initio calculations. *Phys. Rev. B* **65**, 165118.
- Angell C. A., Cheeseman P. A. and Tammaddon S. (1982) Pressure enhancement of ion mobilities in liquid silicates from computer simulation studies to 800 kbars. *Science* **218**, 885–887.
- Angell C. A., Cheeseman P. A. and Kadiyala R. R. (1987) Diffusivity and thermodynamic properties of diopside and jadeite melts by computer simulation studies. *Chem. Geol.* **62**, 83–91.
- Belonoshko A. B. and Dubrovinsky L. S. (1996) Molecular and lattice dynamics study of the MgO–SiO₂ system using a transferable interatomic potential. *Geochim. Cosmochim. Acta* **60**, 1645–1656.
- Boyett M. and Carlson R. W. (2005) ¹⁴²Nd evidence for early (>4.53 Ga) global differentiation of the silicate earth. *Science* **309**, 576–581.
- Bryce J. G., Spera F. J. and Stein D. J. (1998) Pressure dependence of self-diffusion in the NaAlO₂–SiO₂ system: compositional effects and mechanisms. *Am. Mineral.* **84**, 345–356.
- Canup R. M. (2004) Formation of the Moon. *Ann. Rev. Astron. Astrophys.* **42**, 441–475.
- Car R. and Parrinello M. (1985) Unified approach for molecular dynamics and density-functional theory. *Phys. Rev. Lett.* **55**, 2471–2474.
- Cohen A. J., Mori-Sánchez P. and Yang W. (2008) Insights into current limitations of density functional theory. *Science* **321**, 792–796.
- Clare B. W. and Kepert D. L. (1991) The optimal packing of circles on a sphere. *J. Math. Chem.* **6**, 325–349.
- Corgne A., Liebske C., Wood B. J., Rubie D. C. and Frost D. J. (2005) Silicate perovskite-melt partitioning of trace elements and geochemical signature of a deep perovskitic reservoir. *Geochim. Cosmochim. Acta* **69**, 485–496.
- de Koker N. P., Stixrude L. and Karki B. B. (2008) Thermodynamics, structure, dynamics, and freezing of Mg₂SiO₄ liquid at high pressure. *Geochim. Cosmochim. Acta* **72**, 1427–1441.
- de Koker N. (2010) Structure, thermodynamics, and diffusion in CaAl₂Si₂O₈ liquid from first-principles molecular dynamics. *Geochim. Cosmochim. Acta* **74**, 5657–5671.
- Della Valle R. G. and Andersen H. C. (1992) Molecular dynamics simulation of silica liquid and glass. *J. Chem. Phys.* **97**, 2682–2689.
- Dempsey M. J. and Kawamura K. (1984) Molecular dynamics simulation of the structure of aluminosilicate melts. In *Progress in Experimental Petrology* (ed. C. M. B. Henderson). Natural Environment Research Council, Manchester, UK, pp. 49–56.
- Ghiorso M. S., Nevins D., Cutler I. and Spera F. J. (2009) Molecular dynamics studies of CaAl₂Si₂O₈ liquid. II. Equation of state and a thermodynamic model. *Geochim. Cosmochim. Acta* **73**, 6937–6951.
- Ghiorso M. S. and Kress V. C. (2004) An equation of state for silicate melts. II. Calibration of volumetric properties at 10⁵ Pa. *Am. J. Sci.* **304**, 679–751.
- Ghiorso M. S. (2004) An equation of state for silicate melts. III. Analysis of stoichiometric liquids at elevated pressure: shock compression data, molecular dynamics simulations and mineral fusion curves. *Am. J. Sci.* **304**, 752–810.
- Ghiorso M. and Spera F. (2009). Large scale simulations. In *Rev. Mineral. Geochem.*, vol. 71 (eds. R. Wentzcovitch and L. Stixrude). Mineralogical Society of America, pp. 437–463.
- Guillot B. and Sator N. (2007a) A computer simulation study of natural silicate melts. Part I: low pressure properties. *Geochim. Cosmochim. Acta* **71**, 1249–1265.
- Guillot B. and Sator N. (2007b) A computer simulation study of natural silicate melts silicate melts. Part II: high pressure properties. *Geochim. Cosmochim. Acta* **71**, 4538–4556.

- Halliday A. N. (2008) A young Moon-forming giant impact at 70–110 million years accompanied by late-stage mixing, core formation and degassing of the Earth. *Philos. Trans. R. Soc. A* **366**, 4163–4181.
- Hamann D. R. (1996) Generalized gradient theory for silica phase transitions. *Phys. Rev. Lett.* **76**, 660–663.
- Hofer O. C. and Ferreira R. (1966) Covalent and ionic bond orders: applications to the alkali halide molecules. *J. Phys. Chem.* **70**, 85–94.
- Karki B. B. and Stixrude L. P. (2010) Viscosity of MgSiO₃ liquid at Earth's mantle conditions: implications for an early magma ocean. *Science* **328**, 740–742.
- Kite E. S., Manga M. and Gaidos E. (2009) Geodynamics and rate of volcanism on massive Earth-like planets. *Astrophys. J.* **700**, 1732–1749.
- Kohn W. and Sham L. J. (1965) Self-consistent equations including exchange and correlation effects. *Phys. Rev.* **140**, A1133–A1138.
- Kottwitz D. A. (1991) The densest packing of equal circles on a sphere. *Acta Crystallogr.* **A47**, 158–165, Erratum, p. 851.
- Kresse G. and Furthmüller J. (1996) Efficient iterative schemes for ab initio total-energy calculations using a plane-wave basis set. *Phys. Rev. B* **54**, 11169–11186.
- Kubicki J. D. and Lasaga A. C. (1990) Molecular dynamics and diffusion in silicate melts. In *Adv. Phys. Geochem.*, vol. 6 (eds. I. Kushiro and L. Perchuk). Springer-Verlag, New York, pp. 1–50.
- Labrosse S., Hernlund J. and Coltice N. (2007) A crystallizing dense magma ocean at the base of the earth's mantle. *Nature* **450**, 866–869.
- Lacks D. L., Rear D. B. and Van Orman J. A. (2007) Molecular dynamics simulation of viscosity, chemical diffusivities and partial molar volumes of liquids along the MgO–SiO₂ join as functions of pressure. *Geochim. Cosmochim. Acta* **71**, 1312–1323.
- Lange R. A. and Carmichael I. S. E. (1987) Densities of Na₂O–K₂O–CaO–MgO–FeO–Fe₂O₃–Al₂O₃–TiO₂–SiO₂ liquids: new measurements and derived partial molar properties. *Geochim. Cosmochim. Acta* **51**, 2931–2946.
- Lapen T. J., Righter M., Brandon A. D., Debaille V., Beard B. L., Shafer J. T. and Peslier A. H. (2010) A younger age for ALH 84001 and its geochemical link to shergottite sources in Mars. *Science* **328**, 347–351.
- Lee S. K., Lin J., Cai Y., Hiraoka N., Eng P., Okuchi T., Mao H., Meng Y., Hu M., Chow P., Shu J. and Li B., et al. (2008) X-ray Raman scattering study of MgSiO₃ glass at high pressure: implication for triclustered MgSiO₃ melt in Earth's mantle. *Proc. Natl. Acad. Sci. USA* **105**, 7925–7929.
- Leech M. (1957) Equilibrium of sets of particles on a sphere. *Math. Gaz.* **41**, 81–90.
- Luo S. N., Akins J. A., Ahrens T. J. and Asimow P. D. (2004) Optical emission of shock compressed MgSiO₃ glass enstatite, olivine, and quartz. *J. Geophys. Res.* **109**, B05205.
- Marx D. and Hutter J. (2009) *Ab Initio Molecular Dynamics: Basic Theory and Advanced Methods*. Cambridge University Press, Cambridge, UK.
- Morgan N. A. and Spera F. J. (2001) A molecular dynamics study of the glass transition in Ca Al₂Si₂O₈: thermodynamics and tracer diffusion. *Am. Mineral.* **86**, 915–926.
- Martin R. M. (2004) *Electronic Structure: Basic Theory and Practical Methods*. Cambridge University Press, Cambridge, UK, 624p.
- Martin B., Spera F. J., Ghiorso M. and Nevins D. (2009) Structure, thermodynamic and transport properties of molten Mg₂SiO₄: molecular dynamics simulations and model equation of state. *Am. Mineral.* **94**, 693–703.
- Matsui M. (1998) Computational modeling of crystals and liquids in the system Na₂O–CaO–MgO–Al₂O₃–SiO₂. In *Properties of Earth and Planetary Materials at High Pressure and Temperature* (eds. M. H. Manghni and T. Yagi). AGU, Washington, DC, pp. 145–148.
- Matsui M. (1996) Molecular dynamics simulation of structures, bulk moduli, and volume thermal expansivities of silicate liquids in the system CaO–MgO–Al₂O₃–SiO₂. *Geophys. Res. Lett.* **23**, 395–398.
- Mattsson A. E. (2002) Density functional theory: in pursuit of the “Divine” functional. *Science* **298**, 759–760.
- McQuarrie D. A. (2000) *Statistical Mechanics*, second ed. University Science Book.
- Meyer H. D. and Worth G. A. (2003) Quantum molecular dynamics: propagating wavepackets and density operators using the multiconfiguration time-dependent Hartree method. *Theor. Chem. Acc.* **109**, 251–267.
- Mosenfelder J. L., Asimow P. D., Frost D. J., Rubie D. C. and Ahrens T. J. (2009) The MgSiO₃ system at high pressure: thermodynamic properties of perovskite, postperovskite, and melt from global inversion of shock and static compression data. *J. Geophys. Res.* **114**, B01203.
- Nevins D. (2009) Understanding silicate geoliquids at high temperatures and pressures through molecular dynamics simulations. Ph. D. dissertation. University of California, Santa Barbara.
- Nevins D. and Spera F. J. (2007) Accurate computation of shear viscosity from equilibrium molecular dynamics simulations. *Mol. Simul.* **33**, 1261–1266.
- Nevins D. and Spera F. J. (1998) Molecular dynamics simulations of molten CaAl₂Si₂O₈: dependence of structure and properties on pressure. *Am. Mineral.* **83**, 1220–1230.
- Nevins D., Spera F. J. and Ghiorso M. (2009) Shear viscosity and diffusion in liquid MgSiO₃; transport properties and implications for terrestrial planet magma oceans. *Am. Mineral.* **94**, 975–980.
- Oganov A. R., Brodholt J. P. and Price G. D. (2000) Comparative study of quasiharmonic lattice dynamics, molecular dynamics, and Debye model applied to MgSiO₃ perovskite. *Phys. Earth Planet. Inter.* **122**, 277–288.
- Oganov A. R., Brodholt J. P. and Price G. D. (2001) The elastic constants of MgSiO₃ perovskite at pressures and temperatures of the Earth's mantle. *Nature* **411**, 934–937.
- Perdew J. P. and Schmidt K. (2001) Jacob's ladder of density functional approximations for the exchange–correlation energy. In *Density Functional Theory and its Applications to Materials* (eds. K. Van Alsenoy, V. E. Van Doren and P. Geerlings). American Institute of Physics, Melville, NY, pp. 1–20.
- Parr R. G. and Yang W. (1995) Density-functional theory of the electronic structure of molecule. *Ann. Rev. Phys. Chem.* **46**, 701–728.
- Poole P. H., McMillan P. F. and Wolf G. H. (1995) Computer simulations of silicate melts. *Rev. Mineral.* **32**, 563–616.
- Rosenfeld Y. and Tarazona P. (1998) Density functional theory and the asymptotic high-density expansion of the free energy of classical solids and fluids. *Mol. Phys.* **95**, 141–150.
- Rustad J. R., Yuen D. A. and Spera F. J. (1990) Molecular dynamics of liquid SiO₂ under high pressure. *Phys. Rev. A* **42**, 2081–2089.
- Rustad J., Yuen D. and Spera F. J. (1992) Coordination variability and the structural components of silica glass under high pressures. *Chem. Geol.* **96**, 421–437.
- Saika-Voivod I., Sciortino F. and Poole P. H. (2000) Computer simulations of liquid silica: equation of state and liquid–liquid phase transition. *Phys. Rev. E* **63**, 011202.

- Sanchez-Valle C. and Bass J. D. (2010) Elasticity and pressure-induced structural changes in vitreous MgSiO_3 -enstatite to lower mantle pressures. *Earth Planet. Sci. Lett.* **295**, 523–530.
- Sasselov D. D., Valencia D. and O'Connell R. J. (2008) Massive terrestrial planets (super-Earths): detailed physics of their interiors. *Phys. Scr. T* **130**, 014035.
- Spera F. J., Nevins D., Ghiorso M. and Cutler I. (2009) Structure, thermodynamic and transport properties of $\text{CaAl}_2\text{Si}_2\text{O}_8$ liquid. Part I: molecular dynamics simulations. *Geochim. Cosmochim. Acta* **73**, 6918–6936.
- Stein D. and Spera F. J. (1995) Molecular dynamics simulations of liquids and glasses in the system $\text{NaAlSi}_3\text{O}_8$ - SiO_2 . Methodology and melt structures. *Am. Mineral.* **80**, 417–431.
- Stixrude L. and Karki B. (2005) Structure and freezing of MgSiO_3 liquid in Earth's lower mantle. *Science* **310**, 297–299.
- Tarnai T. and Gáspár Z. (1987) Multi-symmetric close packings of equal spheres on the spherical surface. *Acta Crystallogr. A* **43**, 612–616.
- Thorne M. S. and Garnero E. J. (2004) Inferences on ultralow-velocity zone structure from a global analysis of *SPdKS* waves. *J. Geophys. Res.* **109**, B08301.
- Urbain G., Bottinga Y. and Richet P. (1982) Viscosity of liquid silica, silicates and aluminosilicates. *Geochim. Cosmochim. Acta* **46**, 1061–1072.
- Valencia D. and O'Connell R. J. (2009) Convection scaling and subduction on Earth and super-Earths. *Earth Planet. Sci. Lett.* **286**, 492–502.
- van Beest B. W., Kramer G. and van Santen R. A. (1990) Force fields for silica and aluminophosphates based on ab initio calculations. *Phys. Rev. Lett.* **64**, 1955–1958.
- Vinet P., Ferrante J., Smith J. R. and Rose J. H. (1986) A universal equation of state for solids. *J. Phys. C Solid State Phys.* **19**, L467–L473.
- Vuilleumier R., Sator N. and Guillot B. (2009) Computer modeling of natural silicate melts: what can we learn from ab initio simulations. *Geochim. Cosmochim. Acta* **73**, 6313.
- Wan J. T. K., Duffy T. S., Scandolo S. and Car R. (2007) First-principles study of density, viscosity, and diffusion coefficients of liquid MgSiO_3 at conditions of the Earth's deep mantle. *J. Geophys. Res.* **112**, B03208.
- Wentzcovitch R. M., Karki B. B., Cococcioni M. and de Gironcoli S. (2004) Thermoelasticity of MgSiO_3 -perovskite: insights on the nature of the earth lower mantle. *Phys. Rev. Lett.* **92**, 018501.
- Wentzcovitch R. and Stixrude L. (2010) Theoretical and computational methods in mineral physics: geophysical applications. In *Rev. Mineral. Geochem.*, vol. 71. Mineralogical Society of America, Washington, DC.
- White S. M., Crisp J. A. and Spera F. J. (2006) Long-term volumetric eruption rates and magma budgets. *Geochem. Geophys. Geosyst.* **7**, Q03010.
- Wilding M. C., Benmore C. J. and Weber J. K. (2010) Changes in the local environment surrounding magnesium ions in fragile MgO-SiO_2 liquids. *EPL* **89**, 26005 (5pp).
- Xu Y. and Koper K. D. (2009) Detection of a ULVZ at the base of the mantle beneath the northwest Pacific. *Geophys. Res. Lett.* **36**, L17301.
- Zwanzig R. (1983) On the relation between self-diffusion and viscosity of liquids. *J. Comput. Phys.* **79**, 4507–4508.

Associate editor: Michael Toplis